UNIVERSITY OF CALIFORNIA,

IRVINE

Probing Interactions at the Nanoscale by Ion Current through Nanopores and Nanovoids

DISSERTATION

submitted in partial satisfaction of the requirements

for the degree of

DOCTOR OF PHILOSOPHY

in Physics

by

Trevor Patrick Gamble

Dissertation Committee:

Professor Zuzanna S. Siwy, Chair

Professor Phil Collins

Professor Reginald Penner

2014

DEDICATION

To

Mom, LaDonna Gamble

TABLE OF CONTENTS

LIST OF FIGURES

List of Tables

ACKNOWLEDGMENTS

This body of work is the result of large amounts of help from people who were, and have become, very important to me.

My advisor, employer, teacher, and councilor Zuzanna Siwy has been a stay in my graduate school career since my first experiment. During highs and lows, successes and failures, Zuzanna has been available in person or through email 24 hours a day, seven days a week. Always. She has seen me grow from a green yet motivated young researcher to the experienced, thesis writing, senior graduate student that I am today. I look back at the service that she has done for me, and I am impressed at the patience and time that she invested in my life. Before joining her laboratory, I interviewed a few current students. They said that she is a great advisor. They were wrong; Zuzanna is extraordinary.

My committee members Dr. Phil Collins and Dr. Reginald Penner have been very helpful over the past few years. Due to our bi – weekly meetings, I have had ample opportunity to bounce ideas off the two of them, or ask questions. My projects have been modified many times after insight from these specialists. Rare is it that graduate students are given free access to experts in a field as often as I had, in such a comfortable atmosphere. I do believe these two to be important characters in the story of my graduate school career, and am honored to have them on my committee.

I must also acknowledge my co – workers. Tim Plett has been a wonderful addition to my life the past year or so of my graduate career. After a few months of training, he became an active contributor. I often ask him for help more than the other way around it seems now. I have confidence in his ability to become a great success within our laboratory. I have had many wonderful conversations with my co – workers that didn't share the same project with me over the years. These moments are important to me. I like science, but am grateful to enjoy the scientists around me. Greg Zicarelli, Gael Nguyen, Laura Innes, Steven Buchsbaum, Timothy Ma, Matthew Schiel, Matthew Pevarnik, Crystal Yang, Justin Menetrina, Matthew Powell are a few of the friends I have made while working in our laboratory.

The UC Irvine Department of Physics and Astronomy has been a consistent supporting force for me. Any issue that I ever had, that could be solved with their help, was solved with no questions asked. I thank them for that. I also acknowledge the American Chemical Society, American Physical Society, and John Wiley & Sons for letting me use their figures.

CURRICULUM VITAE

Trevor Gamble

2009	B.S. in Physics, University of Michigan, Flint
2009-2011	Teaching Assistant, Physics, University of California, Irvine
2010-2014	Teaching Assistant, Physics University of California, Irvine
2011	M.S. in Physics, University of California, Irvine
2014	Ph.D. in Physics, University of California, Irvine

FIELD OF STUDY

Physics

PUBLICATIONS

Gamble, T., Gillette, E., Lee, S. B. & Siwy, Z. S. Probing porous structure of

Single manganese oxide mesorods with ionic current. J. Phys. Chem. C 117, 24836 – 24842 (2013).

Gamble, T. *et al.* Rectification of ion current in nanopores depends on the type of monovalent cations: Experiments and modeling. *J. Phys. Chem. C* **118,** 9809–9819 (2014).

ABSTRACT OF THE DISSERTATION

Probing Interactions at the Nanoscale by Ion Current through Nanopores and Nanovoids

By

Trevor Gamble

Doctor of Philosophy in Physics

University of California, Irvine, 2014

Professor Zuzanna Siwy, Chair

Polymer nanopores offer themselves as excellent test beds for study of phenomena that occur on the nano – scale, such as Debye layer formation, surface charge modulation, current saturation, and rectification. Studying ions interactions within the Debye layer, for example, is not possible on the micro – scale, where the pore diameter can be 100 times the size of the zone where interactions of interest occur. However, in our nanopores with an opening diameter less than 10 nm, a slight change of the Debye length can lead to drastic changes of the recorded ion current.

Here we present our nanopores' use as a tool to study geometrical and electrochemical properties of porous manganese oxide. There is great value in studying nano – scale properties of this material because of its importance in lithium ion batteries and newly developed nano – architectures within supercapacitors. We electrodeposited manganese oxide wires into our cylindrical nanopores, filling them completely. In this use, nanopores became a template to probe properties of the embedded material such as surface charge, ion selectivity, and porosity. This information was then reported to the Energy Frontier Research Center (EFRC) collaboration, so that other groups can

incorporate these recently discovered characteristics into future their nano – architecture design.

Additionally, we constructed conical nanopores to study interactions between the surface charges found on the walls and alkali metal ions. In particular we looked at lithium, as it is the electrochemically active ion during charge cycling in EFRC energy storage devices. We attempted to reveal lithium ion's affinity to bind to surface charges. We found this binding led to lowering of the effective surface charge of the pore walls, while also decreasing lithium's ability to move through channels or voids that have charged walls. In connection to manganese oxide, a porous, charged material with voids, information on lithium's interaction with these charges is paramount.

Introduction

Nanopores are holes created synthetically or biologically that allow the passage of material, usually ions, through a thin membrane. Nanopores are found in a wide range of membranes, from ultra-thin single layer graphene samples[1,2,3,4] to tens of micrometers thick polymer templates[5,6,7,6,8,9]. Biological nanopores, essential to almost all life on earth, serve as selective gates in lipid bilayers. These nanopores are formed by proteins[10]; a common example being voltage gated channels for nerve signaling and heart muscle function. Synthetic nanopores come in various forms, each with their own unique fabrication procedures. Nanopores are constructed from materials such as polymers[5,9,11,12,13], silicon nitride[14–17], and alumina[18–20]. Newest to this group are graphene nanopores. This material, and its nanopores, has recently found the attention of many research laboratories worldwide[1,21].

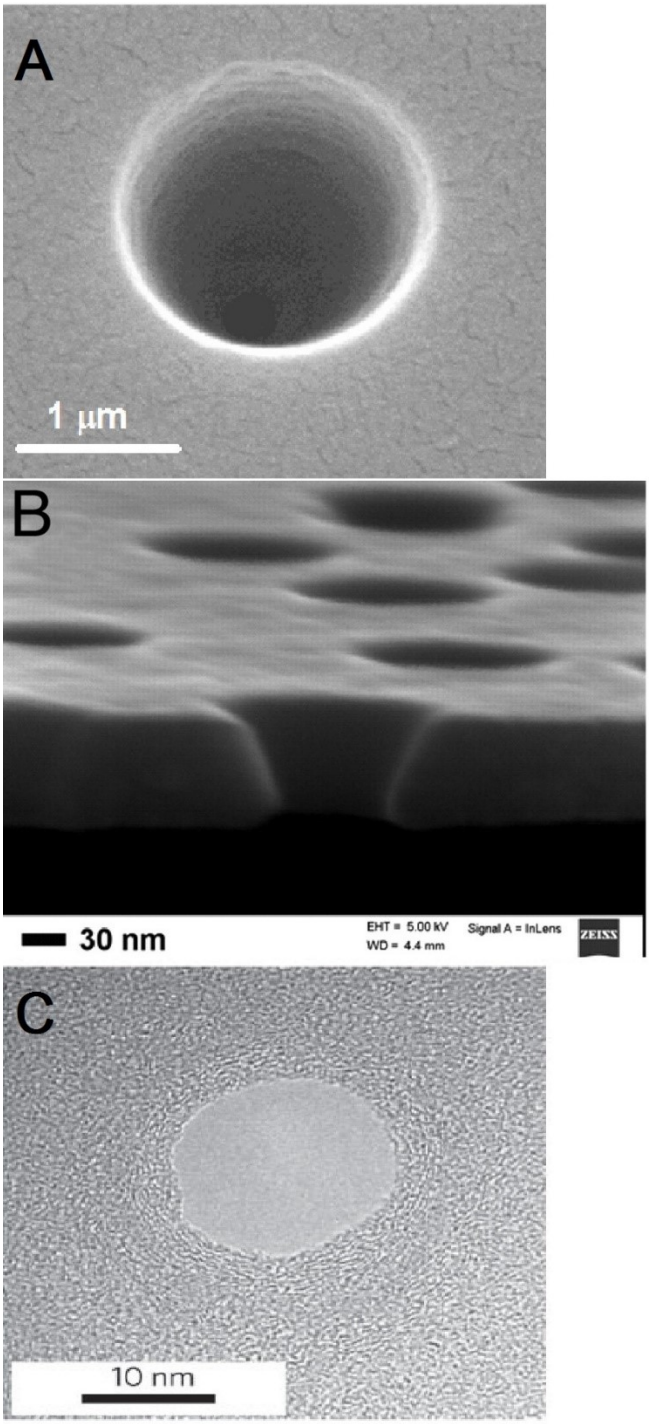

Figure 0.01 – (A) SEM image of a conical nanopore etched through a PET (polyethylene terephthalate) membrane. The membrane was 12 micrometers thick. (B) SEM image of nanopore etched through silicoin nitride membrane, with thickness of approximatly 90 nm. (C) TEM of nanopore bored through a single layer of graphene. (A), (B), and (C), courtasy of refrences [17], and [2] respectivly.

Due to the high surface area to volume ratio, scientists use nanopores to uncover interactions that occur between ions, DNA, viruses, and material interfaces, in ways that were not previously possible with micro - scale devices[22]. Synthetic and biological nanofluidic devices are fabricated and subjected to stimuli in ways that allow experimentalists control transport of ions in solution, and elucidate nano – scale phenomena useful for technology improvements in biology, material science, and electronics. Biologists and biophysicists have great interest in learning physical and chemical phenomena underlying function of biological channels, e.g. in order to perfect techniques that manipulate gating, for use in the medical field. Drug delivery is often dependent on protein nanopores, as they might regulate the access medicine has to the inside of a cell[23]. For man-made nanopores, DNA sequencing is a viable application, accomplished by reading the conductance across the nanopore while a single DNA strand translocates through the opening[24]. Each base, as it passes through the pore, disturbs the current across the nano - gap in a unique way, allowing the experimenter to identify the sequence of the strand.

In our laboratory we use polymer nanopores[25]. We test membranes whose nanopore density ranges billions of per square centimeter, down to a single pore per membrane. Their shape and dimensions are easily modified, and our polymers can be modeled accurately in several continuum and molecular dynamics based packages. These traits make our polymer nanopores excellent test beds to study properties of materials, molecules, or ion interactions within nanopore during experiment.

Chapter 1

Nanopore Fabrication and Characterization

Nanopores used in the presented research were created in 12 micrometer thick polyethylene terephthalate (PET) films through the use of the track-etch technique[26]. The name comes from the two main steps of fabrication. A track, or damage track, is formed inside a polymer foil by bombarding it with high-energy heavy ions, which pass completely through the foil, agitating the polymer chains. Uranium and gold are species typically used for this purpose. Formation of damage tracks was discovered by E.C.H. Silk through TEM (Transmission Electron Microscopy) of mica bombarded with daughter ions from the fission of U235[27]. These tracks are useful in that they etch quicker than the bulk material when exposed to etchant solution, allowing pores of various shapes and diameters to be created without compromising the entire film. In this chapter we will show how to transition from a pristine PET foil into a functioning nanopore suited for experiment. These nanopores are used to discover behavior about materials deposited inside them, as well as uncovering interactions of ions with the PET surface itself. The unique property of the track-etching approach is one-to-one correspondence between the number of ions that bombard the film and the number of obtained pores after the etching process. In the research presented here, we used single pores when collecting data, and multipore samples for optimization of deposition process when the polymer membranes were used as a template.

1.1 Damage Tracks

Nuclear damage tracks created by bombardment of heavy ions is the first step to creating our nanopores. Research has shown that when the total kinetic energy of the energetic ions is sufficiently high, these tracks extend through the entire membrane, with a diameter less than 5 nm at any given point. The damage track is characterized by the presence of agitated and displaced atoms[28]. The polymer chains containing these atoms are more chemically reactive than neighboring chains outside the damage track, which is an important requirement for the track – etch process.

The ion bombardment is performed at the GSI Helmholtzzentrum für Schwerionenforschung in Darmstadt, Germany. This facility has an ion accelerator set up that controls the number and energy of ions that pass through each polymer membrane[29]. We receive samples with a record of the number of damage tracks, the energy of the culprit ion, and the type of ion. All ions used for irradiation at GSI have energy of 11.4 MeV/u.

The heavy ion interacts with either the electrons or the nucleus of polymer atoms as it passes through. These interactions both disturb and agitate the bonds, creating chemically reactive sites. The first type of interactions is electronic. The second system occurs at lower energies, and is described as ion – atom collision. A gold ion for example can be ionized to the charge of +25e. As the ion passes through the polymer film it interacts with the medium's electrons, depositing energy, causing promotions and ejections. As the gold ion loses energy it slows down. This allows the ion to remove electrons from the medium in order to fulfil the need to reduce its high ionic charge.

However, this charge reduction reduces the ions effectiveness in dissipating energy through electromagnetic interactions with the medium's electrons. As the ion loses energy, its cross section, a term used to describe a particles probability to interact with matter, for ion-atom interactions increases. This strong interaction causes entire atoms to be removed from their place in polymer chains, decreasing the overall strength of the chain, and therefore leading to preferential etching in the area.

There are two theoretical models which were developed to explain the formation of damage tracks: the thermal spike model and the Coulomb spike model[30,31]. In both models a high energy ion passes through a medium, disturbing the resident electrons. These theories are sufficient to explain the formation of damage tracks in PET, as the ions used for irradiation at GSI never have their initial energy reduced enough to have a substantial ion-atom cross section. Thus, the formation of the damage track must be explained by ion-electron interactions that take place during the passage of the ion through the material.

In the thermal spike model the high energy ion passes through the material and promotes electrons to a higher energy state. The ion itself loses energy in this process. Promoted electrons return to their ground state eventually by emitting energy in the form of a photon, or phonon. In the thermal spike model a phonon is released, dispersing vibrational energy. Each atom in the track receives a large amount of thermal energy, and quickly disperses this energy into neighboring atoms. This large release of vibrational energy followed by near instant cooling leaves the track atoms significantly displaced from their original position. Preferential etching is due to the fact that atoms are out of their initial assigned positions within the polymer chain, weakening affected

chains. Evidence in support of this model comes from the ability to repair damage tracks through annealing. It has been shown that PET damage tracks can be repaired through annealing[32], which allows the track atoms enough energy to return to their initial and energetically favorable positions within the polymer chain. This supports the idea that the tracks are created through high deposition of energy followed by rapid cooling.

The second explanation for damage tracks is known as the Coulomb spike model, also known as the ionization spike model. Atomic displacements still drive the formation of the damage track, however, the atomic movement is due to Coulomb repulsion[30]. The heavy ion travels through the material ionizing atoms by depositing energy into their electrons, causing one or more to be ejected from the host atom. In the wake of the heavy ion, atoms suddenly feel strong electronic repulsion from each other due to loss of their electrons. Figure 1.1.1 is a scheme of the relationship between the weakened polymer bonds and the heavy ion path. Ion tracks are visible in TEM micrographs in Figure 1.1.2. Their images are created by staining ultrathin PET with OsO_4 or RUO_4. This staining provides contrast between the pristine PET membrane and the damage tracks containing agitated polymer chains. More detailed cause of damage tracks remains unknown, but it is largely believed to be a combination of the previous two theories.

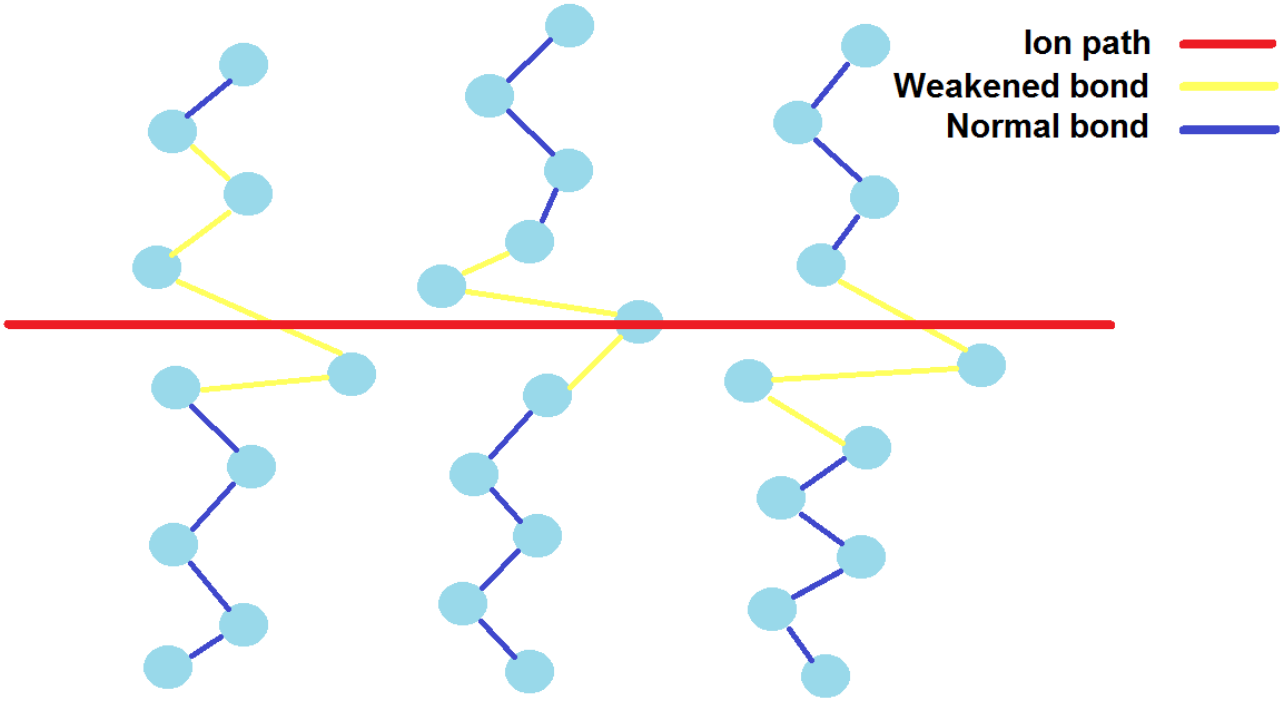

Figure 1.1.1 – Three PET polymer chains are shown, with an impact path from a heavy ion. The red line represents the path of the heavy ion as it travels through the polymer. The damage track consists of weakened bonds. These bonds are the result of energy deposited (through interactions with electrons) from the heavy ion into the polymer chains.

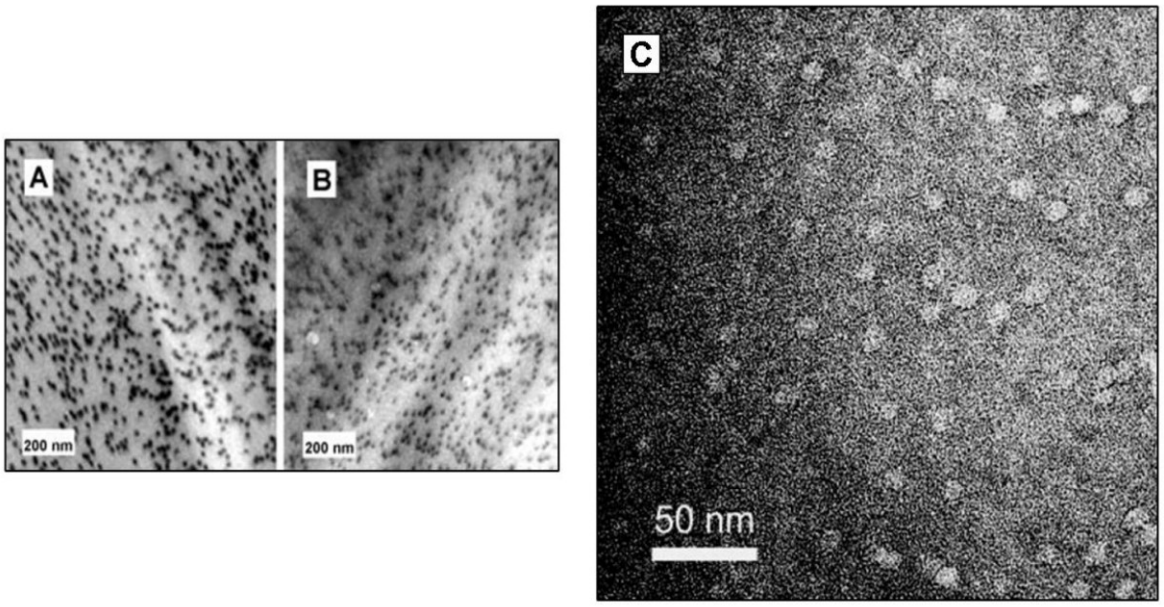

Figure 1.1.2 – TEM of damage tracks caused by heavy ions in PET films. The track density is 5 x 10^{10} ions / cm^2. (A) Contrast was created by using RuO_4 stain for one hour using 2640 MeV uranium ions. (B) Contrast was created by a 24 hour OsO_4. (C) RuO_4 stain showing tracks created by 2310 MeV lead ions. Reproduced with permission from John Wiley and Sons.

1.2 Wet Etching

Damage track creation is the beginning step for the formation of pores by the track-etching technique. To achieve pores with tailored geometries and opening diameter, several more steps are needed. After heavy ion bombardment, a PET film is exposed on both sides to ultraviolet light. A 365 nm light source (UVP UVGL – 25) is used to illuminate the foil for one hour on both sides. The cause for ultraviolet light's effect on polymer structure is not fully understood, but it is known that light only affects polymer chains in damage tracks[33]. The bulk PET membrane is not altered significantly. Also known is the importance of O_2 molecules[33,34]. Ultraviolet radiation has no effect on PET structure in argon or nitrogen atmosphere[33]. This selective influence allows the use of a dose of radiation to be used to further increase the difference between bulk and

track etch rates, shortening the time it takes to fabricate pores. An etch rate increase of ~400% is typically observed for one hour exposure. It has been also noticed that over exposure to ultraviolet radiation causes inconsistent pore etching and less stable pores e.g. fluctuations of ion current values. Origin of these effects is not yet known.

After ultraviolet radiation the membrane is ready for the wet etch process. The chemistry used is an interaction between sodium hydroxide solution and the ester bonds of PET polymer chains. The temperature and molarity of NaOH are varied depending on the desired pore geometry, but the chemical reaction is alkaline hydrolysis for any shaped nanopore. As seen in Figure 1.2.1 the hydroxide ion attacks the PET chain at the ester bond. This produces a waste product ethylene glycol, and leaves an exposed carboxyl group at the site of attack. This carboxyl group is very important for our nanopores, as it is the source of surface charge above pH 3.8. The second step is another attack at the ester bond. This produces another waste product, sodium salt of terephthalic acid, and returns the polymer chain back to its original state minus one monomer. The etching process will continue until the sodium hydroxide supply is exhausted, or the membrane is dissolved entirely. 0.5 M NaOH solution at 70° C will etch a PET foil completely when left to react overnight. Later we will show how time or current recordings are used to determine when to halt the wet etch process.

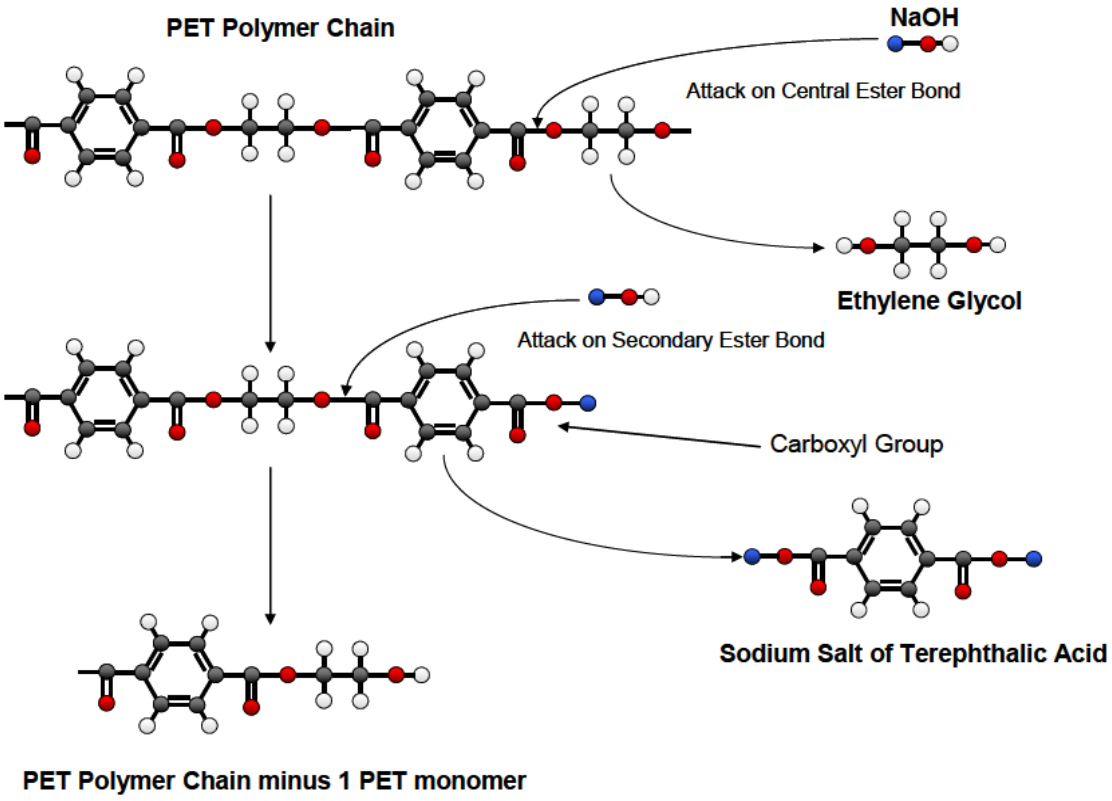

Figure 1.2.1. - Hydrolysis of PET polymer chains, which occurs during the etching process. After a single attack at the ester bond by an hydroxide ion, an ethylene glycol molecule is released, leaving a carboxyl group exposed. A second attack leaves the PET polymer chain identical to its previous state, minus one monomer. Image courtesy of E. Kalman.

Geometry of the pore is decided based on the goal of the experiment, and the etching parameters are adjusted accordingly. The parameters we can use to tailor pore geometry are temperature, molarity of the etchant, and also which sides the etchant has access to. First we will discuss etchant access. In order to obtain conically shaped PET nanopores a concentrated solution of NaOH is added to only one side of the membrane. An acidic solution called the “stopping solution”, which will be discussed in the next paragraph, is added to the other side. For cylindrical and double conical pores the

etchant is added to both sides with symmetric concentration. Temperature is another important parameter which we use to tailor our nanopore geometry during the etching process. The track etch rate is significantly more sensitive to temperature changes of the etchant solution than the bulk PET polymer. The etch rate for the track increases from 150 nm / minute to 1200 nm / minute when the temperature is increased from 20º to 70º C, increasing the ratio of track etch to bulk etch to 700. This allows, as seen in Figure 1.1.2, the track to etch through “instantly,” permitting the etchant to attack the bulk PET that surrounded the track, creating a slowly growing cylindrical shape. The molarity of the sodium hydroxide solution controls both the bulk and track etch rate. Any increase in molarity of NaOH leads to a greater bulk and track etch rate. However, the bulk membrane is more sensitive to change in NaOH concentration. Thus to obtain conical pores in PET the etching is performed in 9 M NaOH and at room temperature, where the bulk etch rate was measured to be ~2.13 nm / minute and the track etch is 150 nm / minute. In the course of etching, the pore opening directly exposed to the 9M NaOH is typically ~500 nm in diameter after 120 minutes of etching. Typically a breakthrough occurs after two hours of etching. This is when the NaOH solution has etched a path through the foil and the tip diameter of the pore begins to widen. This important step is discussed in the next section.

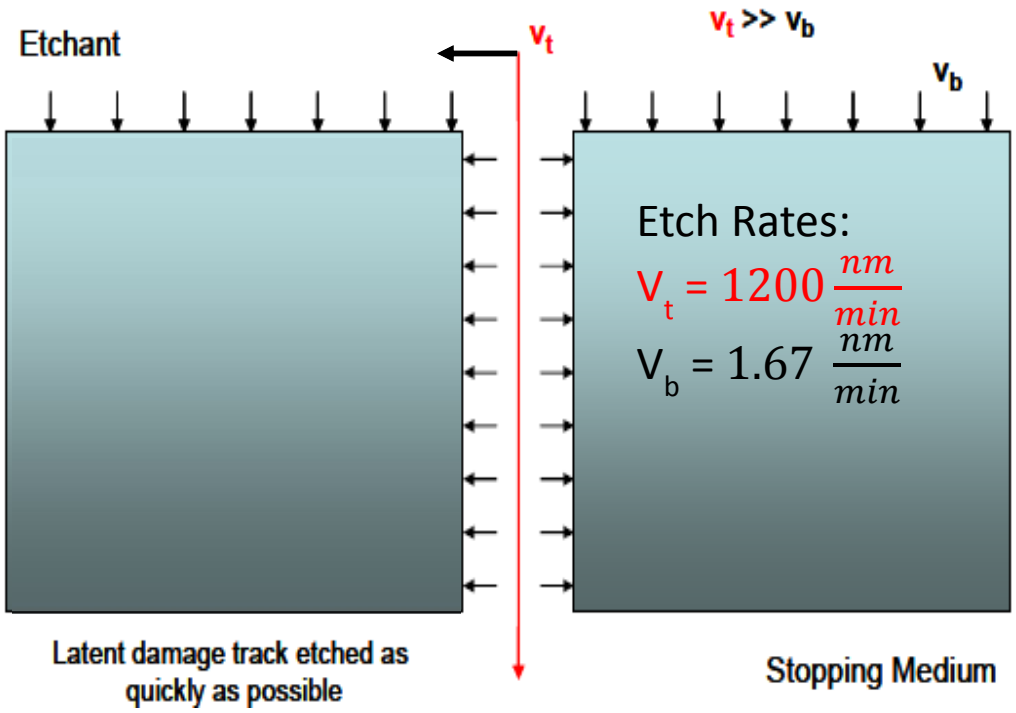

Figure 1.2.2 – Scheme of cylindrical nanopore in PET being etched in 0.5 M NaOH, at 70 ºC. The large difference between the track and bulk etch rates allow the pore geometry to become cylindrical, with a diameter that increases at the rate of 50 nm / hour.

Controlling the tip diameter of a conically etched pore is done by an empirically determined approach. Figure 1.2.3 shows a diagram of the etching conditions. The side of the foil that is to have the wide opening of the nanopore is exposed to sodium hydroxide at a concentration of 9M. The side that is to be the tip of the nanopore contains 1M potassium chloride and 1M formic acid. This is referred to as stopping solution.

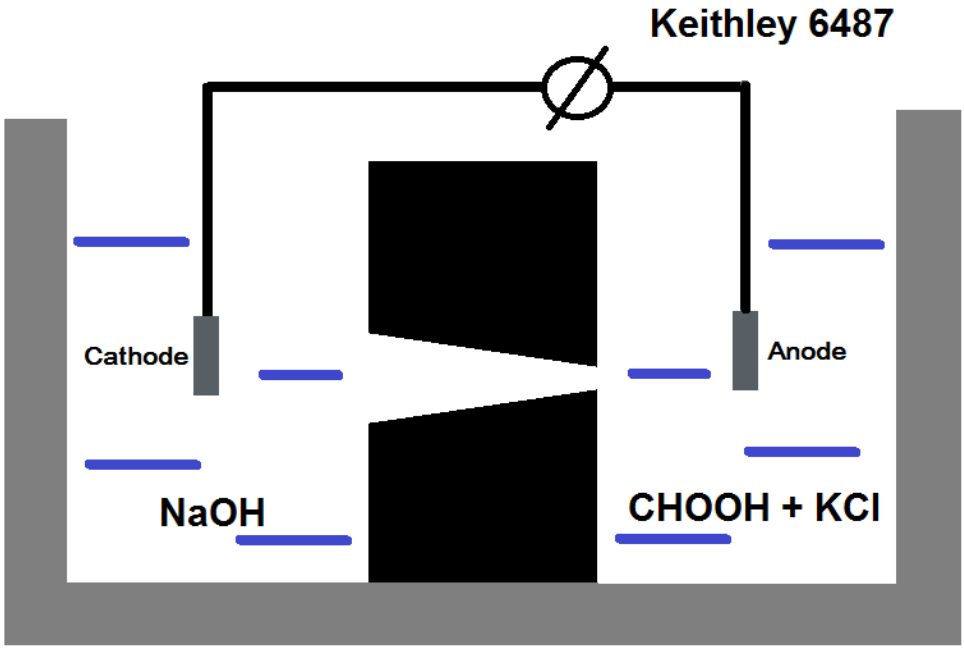

Figure 1.2.3 – Setup of a conductivity cell during the wet etch process. 9M NaOH is the active etchant, while 1M Formic acid is used to slow the etching once initial breakthrough pore occurs. The left electrode is held at positive potential with respect to the right electrode, to pull hydroxide ions out of the pore during breakthrough, further slowing the etching process.

The purpose of the formic acid is to react with the hydroxide ions upon breakthrough, when the solutions are allowed to mix. This slows the etching process by lowering the pH inside the tip of the pore. The reaction for the formic acid and hydroxide ions is

$$OH^- + HCOOH \rightarrow H_2O + HCOO^- \qquad (1.2.1)$$

which produces a formate ion and a water molecule as waste products. An electric field is also utilized to slow the etch rate of the tip of the nanopore. A 1V potential difference

is applied across the pore as seen in Figure 1.2.3. This electrophoretically drives hydroxide ions out of the tip of the pore, and chloride ions into the narrow opening. This additional lowering of the pH further slows down the process of tip enlargement.

The method for determining the tip opening is based on recording the current through the pore observed during the etching process, and afterward. Seen in Figure 1.2.4, the beginning of the breakthrough is noticed as an increase in current from zero to a finite value. Through preparation of many pores we established that a breakthrough current of ~200 pA indicates the nanopore has an opening diameter of a few nanometers. If a larger pore size is desired the etching is allowed to continue until current up to 1 nA is reached.

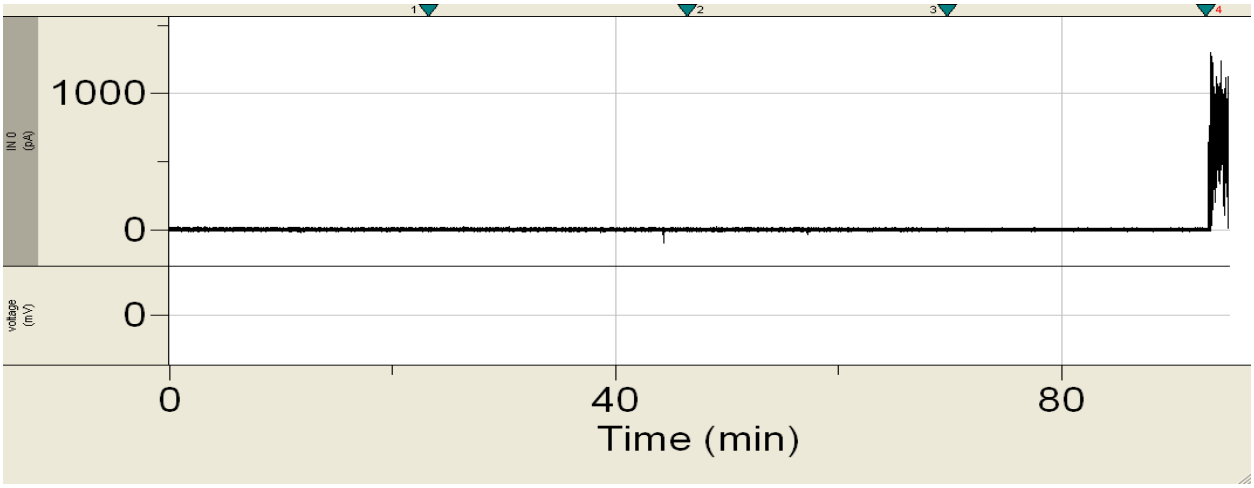

Figure 1.2.4 – Example of a current recording during pore breakthrough. Little to no current is measured until pore breakthrough, where NaOH begins to enlarge the diameter of the tip side of the conical pore. During this process a rapid increase in current is seen. A typical stopping point is 200 pA, but current up to 1 nA currents are allowed if a larger tip diameter is desired.

Due to the asymmetry of composition and molarity of solutions on the two sides of the membrane, together with the neutralization reaction occurring at the narrow opening, the observed current is not directionally proportional to the final tip diameter. A sizing of

the pore after the etching process is complete is needed. This is done in symmetric salt conditions, and results in an estimate of the pore opening diameter. Cylindrical pores are etched using a different process. The same track – etch membrane is used, however the membrane is not etched inside a conductivity cell. The foil is placed in a container filled with 0.5M NaOH heated to 70° Celsius. This container is kept at constant temperature by use of a water bath as seen in Figure 1.2.5.

Figure 1.2.5 – Water bath setup for PET cylindrical pore etch. 0.5M NaOH solution at 70° C is used. The damage track is etched at a rate of 1200 nm / minute and the bulk polymer at 1.67 nm/ minute under these conditions.

The membrane is placed loosely inside a coiled wire to prevent it from sticking to the bottom or side of the container, allowing the etchant access to both sides of the membrane, as required for a uniform etch. Under these conditions the diameter of the pore grows at a rate of 100 nm / half an hour.

Pore sizing is done as shown in Figure 1.2.6. For both conical and cylindrical pores 1M KCl is placed in both cell compartments. By recording the current-voltage curves through the pore, the pore resistance can be calculated. A Keithley picoampmeter is used to apply a voltage across the pore while simultaneously measuring the current

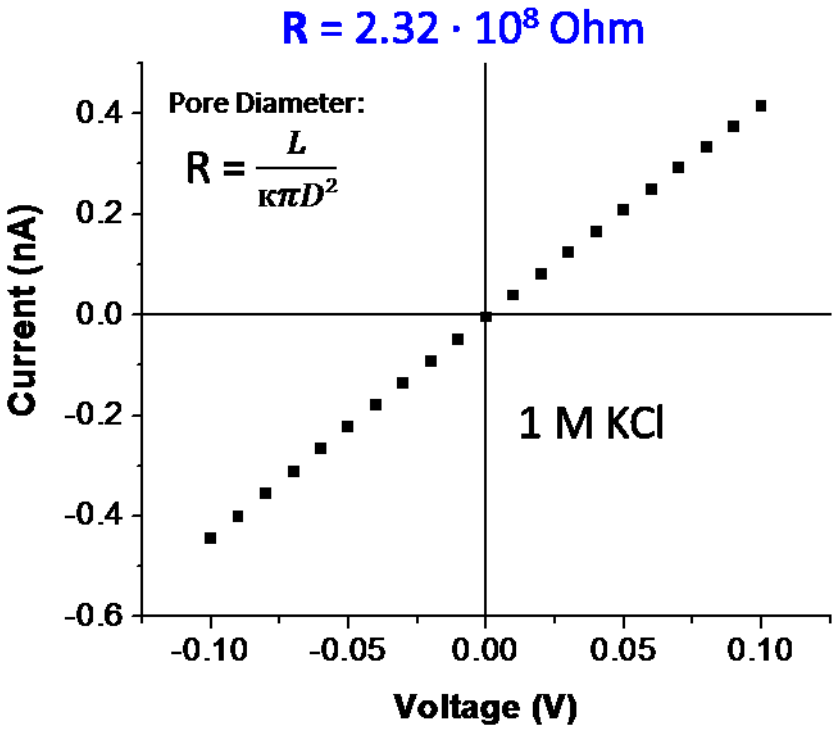

Figure 1.2.6 – Current – voltage data for a cylindrical pore. The equation presented is used to calculate the pore diameter through knowledge of the resistance measured, the length of the pore, and the conductivity of the solution. This example is from a cylindrical pore with a diameter of 82 nm.

passed through. For a cylindrical pore the relationship between diameter and resistance is given by the formula for a cylindrical resistance element:

$$R = \frac{L}{\kappa \pi D^2} \tag{1.2.2}$$

The variables here are κ, the conductivity of the solution, and L the length of the pore. L is always 12 microns for our samples. For a conical pore we use the formula for a conical resistance element,

$$R = \frac{L}{\kappa \pi A b} \tag{1.2.3}$$

derived by use of integration. This approximation is exact for a resistor that is a circular section of a sphere, and becomes more accurate as the opening angle of the cone decreases[33,35]. L again represents the length of the pore, A represents the radius of the large opening of the pore, while b is the radius of the small opening of the pore. The large opening is calculated from the bulk etch rate at room temperature and the duration of the etch, which reduces the equation to one unknown variable. It must be noted that the resistance measured is a combination of several discrete resistances. Each electrode has an inherent resistance as does the bath, or solution, itself. This is depicted in Figure 1.2.6.

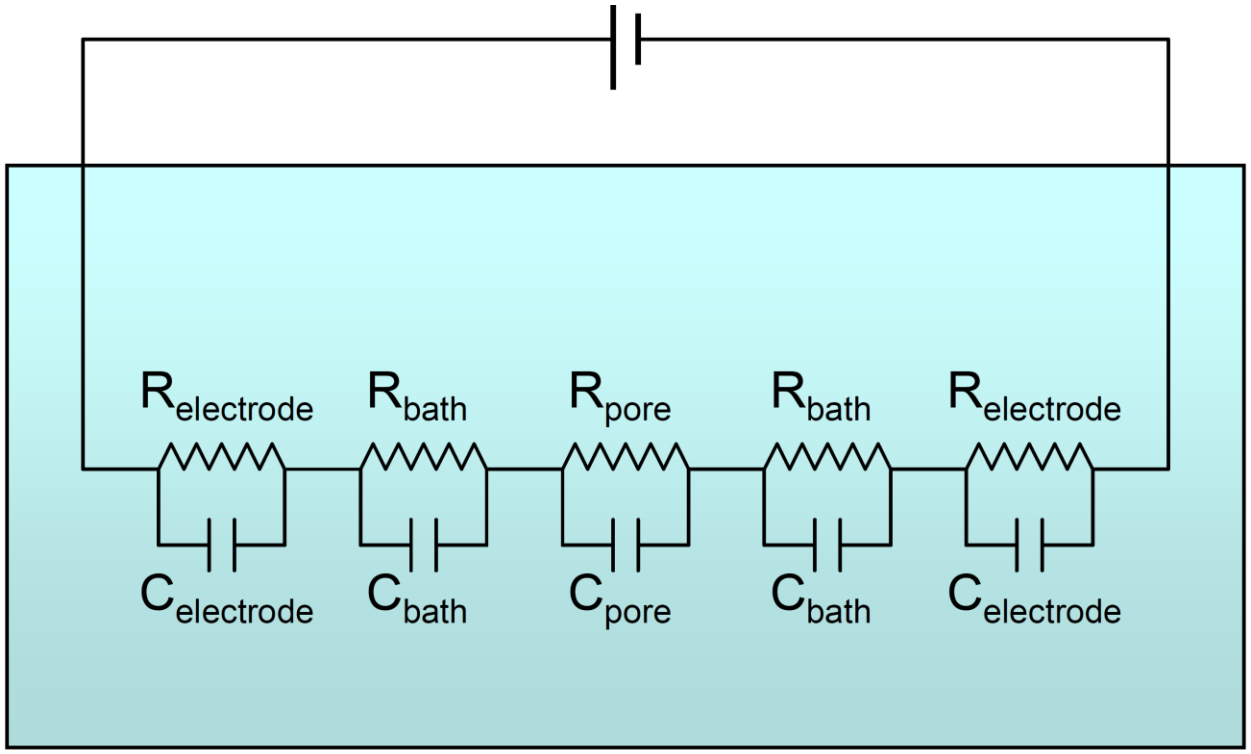

Figure 1.2.7 – Diagram of the various resistances and capacitances seen in our conductivity cells during current measurements through a nanopore. The resistance of the nanopore itself is the dominant factor, and the only major player when using resistance to calculate the size of a nanopore. Image courtesy of E. Kalman.

Ag/AgCl electrodes are known to have resistances below 10 Ohm[36] . Low resistance is one of the properties that make Ag/AgCl popular for use in electrochemical experiments. The resistance of the bath varies depending on concentration and electrolyte used. When sizing pores 1M KCl is used. With dimensions used in our nanopore conductivity cells, an approximate 4 Ohm resistance is expected. Numerically this comes from the conductivity of KCl being 10 S/m at 1M concentration, and by representing the bath as a cylinder of diameter 0.5 cm and 0.5 cm length. The nanopore resistance reaches gigaohms, and therefore dominates, validating our simplification used in our sizing calculation. The process for fabricating multipore samples is identical to the procedure used for preparation of single pores. However using current values to

characterize the pores after creation is very difficult due to the large magnitude of currents. When needed, SEM imaging is used to measure the average pore size in a multipore sample.

Chapter 2

Nanopore Transport and Double layer

Theoretical description of ion transport inside nano-constricted volumes is needed to truly understand the ion current behavior seen in our nanofluidic devices. Subtle changes to the shape or surface charge of a nanochannel can produce very different transport properties. In contrast to biological channels in a cell membrane, simply shaped synthetic nanopores often adhere very closely to predictions made by continuum description of electrostatic interactions and ion current. In this chapter, we discuss theories that have been developed to explain the physics behind ionic current at the nano-scale.

2.1 Debye Double Layer

A charged surface immersed in a solution will modify the distribution and orientation of ions and molecules nearby. In the case of water molecules, the polar nature of water will cause it to rotate itself such that the orientation favors electrostatics. Ions will gather near or move away from the surface, depending on what is favorable energetically. A double layer, also known as a Debye layer, consists of an overall excess of ions, with a preference for ions opposite the surface charge polarity[37]. The Debye layer typically is on the order of 5 – 10 nm. The Debye layer does not play a large role if the channel diameter is large, around a micrometer or greater[38]. However, in our nanopores, the channel diameter may be less than 10 nm. This means the Debye layer plays an important role in ionic currents through the nanopore. Some devices such as the

nanofluidic diode and transistors[25][13,39] only function because of the ability to modulate ionic concentrations by the surface charge and externally applied voltage. The goal of this section is to explain the theory and importance of the Debye layer in our experiments.

Discussion on the prevalence of the Debye layer on the nano-scale must start with the accompanying mathematics. Presented here is the Gouy-Chapman model. The first assumption that must be made is on the distribution of ions inside the Debye layer. As in Figure 2.1.1, we assume a planar surface charge with mobile positive and negative ions outside it. In The Stern layer is also depicted; this layer of immobile ions linearly reduces the potential caused by the surface charge. Our mathematical formulation starts with the potential just outside the Stern layer, which we will refer to the surface potential. The ions will naturally want to minimize their energy within this electric field, so a Boltzmann distribution is used. This is given by

$$\rho(y) = zFC_0[e^{\frac{-zF\emptyset(y)}{RT}} - e^{\frac{zF\emptyset(y)}{RT}}] \quad (2.1.1)$$

where z represents the charge of the ion (+1 for monotonically charged cations and anions, respectively).

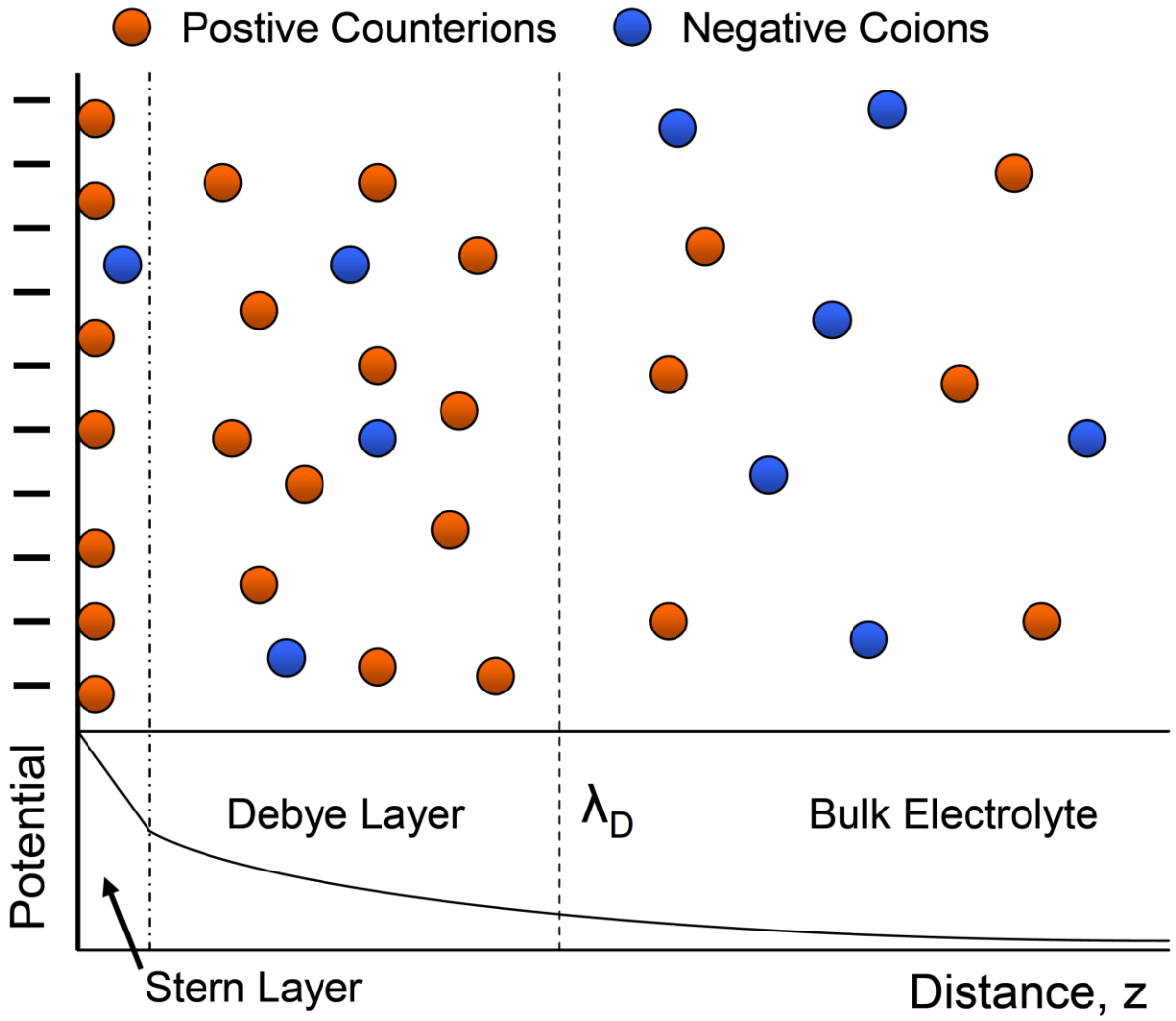

Figure 2.1.1 – Diagram of the Stern layer and Debye layer. As the distance from the charged surface extends beyond the Debye length λ_D, the ion concentration approaches bulk levels. Inside the Debye layer volume, counterion population is increased due to the surface charge and electroneutrality needs. Electric potential decreases from the value at the surface to zero far away from the charged surface. Image courtesy of E. Kalman.

F represents the Faraday constant, the charge of one mole of electrons, equaling 96485 C / mol. C_0 is the bulk concentration of the solution in which the charged surface is immersed. R and T represent the gas constant (8.314 J / K · mol) and temperature, respectively. In the numerator we have the electric potential as a function of y, the

distance away from the surface. For a positively charged ion (positive z) the first term represents positive ions, and the second negative ions. This formula can be simplified by using the trigonometric expression

$$\sinh(x) = \frac{(e^{x} - e^{-x})}{2} \qquad (2.1.2)$$

which simplifies our previous distribution to

$$\rho(y) = -(2zFC_0)\sinh[\frac{zF\emptyset(y)}{RT}] \qquad (2.1.3)$$

If one makes an assumption $\emptyset(y)$ is small, comparable to k_bT, equation 2.1.3 can be simplified to:

$$\rho(y) = \frac{2z^2F^2C_0\emptyset(y)}{RT} \qquad (2.1.4)$$

It is important to recall that the charge density can always be expressed within the Poisson equation, which remains valid no matter the geometry or source of the charge distribution. This equation is

$$\frac{d2}{dy2}\emptyset(y) = -\frac{\rho(y)}{\varepsilon\varepsilon 0} \qquad (2.1.5)$$

or in three dimensional operator form,

$$\nabla^2\emptyset = -\frac{\rho}{\varepsilon\varepsilon_0} \qquad (2.1.6)$$

allows us to combine equations 2.1.4 and 2.1.5 to form a differential equation. The boundary conditions valid for a surface charge in solution containing ions are then inserted. The potential, ø(*y*), must equal zero as *y* becomes large, i.e. as we are moving

away from the surface charge. As *y* approaches zero, ø(*y*) must become the surface potential ø(*y*)$_{surface}$. Applying those boundary conditions and solving the differential equation gives us

$$\emptyset(y) = \emptyset\text{surface } e - \frac{y}{\lambda} \qquad (2.1.7)$$

where λ has units of length and is represented by

$$\lambda = \sqrt[2]{\frac{RT\varepsilon\varepsilon 0}{2z2F2C_0}} \qquad (2.1.8)$$

which is called the Debye length. Mathematically, for low surface potentials where linearization is justified, it represents the value of *y* at which the potential decreased *e* times. Assuming room temperature, z = 1, the Debye length can be simplified to

$$\lambda = \frac{0.3\ nm}{\sqrt{C_0}} \qquad (2.1.9)$$

where c_0 is the bulk electrolyte concentration in moles/liter. The magnitude of the Debye length is often considered a crossing point; within the distance from the surface, the solution contains mostly counterions, and outside often a solution with bulk concentration is assumed. Along with being easy to calculate, this Debye length allows physicists and chemists to decide if the surface charge is a major player in effects (such as measured currents) seen in experiments. Just outside the Debye length, there is still an excess of counter ions, but their number diminishes as the distance from the surface is increased; the excess counter ion concentration decays exponentially with respect to distance from the surface. The Debye layer is important on the nano-scale since its dimensions are comparable to the size of objects such as nanopores. As an example,

we will consider a 12 micrometer long cylindrical nanopore with an opening diameter of 10 nm. With a concentration of 10 mM KCl and room temperature, the Debye layer is calculated to be 3 nm. This means that 84% of the volume of solution inside the nanopore is inside the Debye length. Inside this zone, the concentration of excess counterions is determined by the surface charge and electroneutrality. This allows the possible situation where the concentration of ions inside the channel is determined by the surface charge. The chances of this occurring and magnitude of the effect are dependent on the bulk concentration, the diameter of the pore, and also the surface charge of the channel. The conductivity of the channel indeed often differs significantly from what is expected from the bulk concentration. An expression for the difference in counter-ion and co-ion concentration inside a cylindrical nanopore has been found using a truncation of the Poisson-Nernst-Plank equations[40].

$$C_+(z) - C_-(z) = -\frac{2\sigma(z)}{ea} \tag{2.1.10}$$

This formula gives a concentration difference between positive and negative ions of 0.67 M for a 10 nm diameter pore with a surface charge density of 1 e / nm^2. Let's now consider a conically shaped nanopore whose one opening only is nanoscopic; the cone base has diameter of few hundreds of nm. The Debye layer is thus small in comparison to the base of the pore, but will play a critical role in determination of ion concentrations and conductivity near the tip of a conical nanopore. This is seen in Figure 2.1.2, where it can be seen that the solution in the large opening is not much different from the bulk solution. With a Debye layer of 5 nm and an opening diameter of 500 nm, the Debye layer modified volume is only ~.0004% of the total volume.

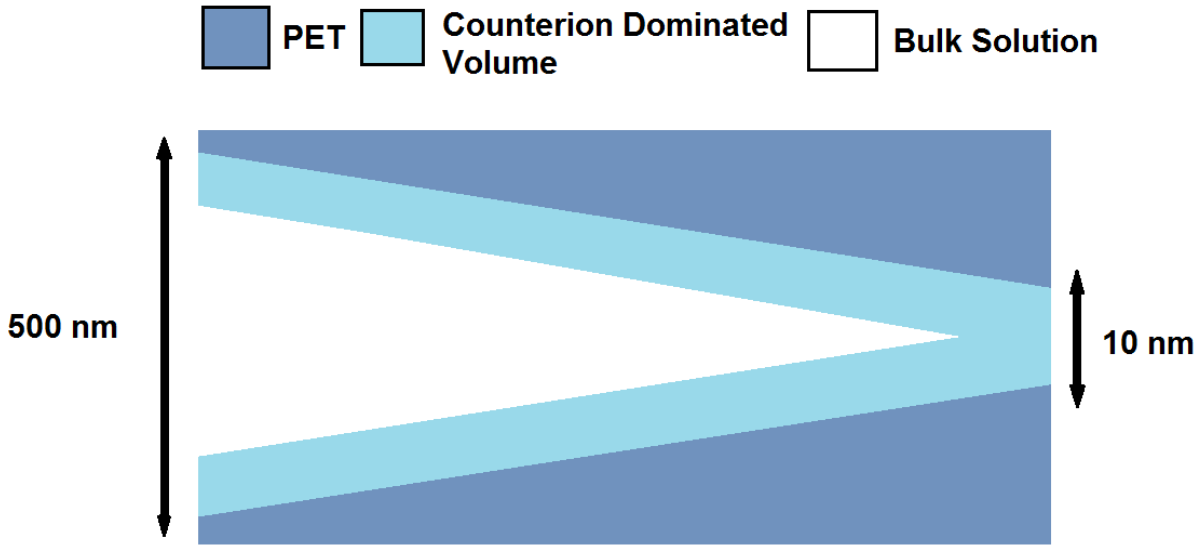

Figure 2.1.2 – Comparison of bulk solution volume and Debye layer volume (counterion dominated) for a conical pore with large opening diameter of 500 nm and small opening diameter of 10 nm. The Debye layer plays a critical role near the tip of the nanopore, where the ion concentration is most effectively modulated by the surface charge. This scheme is not to scale.

However, at the tip of the pore where the dimensions are sub–10 nm, the volume of solution inside the Debye layer can reach 100%. Rectification in our conical nanopores, as described later in this document, only occurs when the Debye layer length is comparable to the radius of the tip of the nanopore. Devices have been created that exploit the designer's control of the polarity and concentration of ions that reside inside the channel. One such example is nanofluidic diodes. These are nanopores that have been modified to have regions of positive and negative surface charge[13]. This pattern enhances rectification producing diode like behavior with almost zero current in the off

state. By varying the geometries and surface charge patterns of nanopores even further, nanofluidic transistors have also been fabricated successfully[25]. The Debye length is tremendously important on the scale at which our nanopore experiments are performed. As such, it must be calculated and taken into consideration when any nanopore science results are discussed.

2.2 Ion Transport and Selectivity

Ions can be forced to move in solution through application of electric potential, pressure difference, concentration gradient, and also difference in temperature. In our laboratory all experiments were performed at room temperature. The amount of solution in each side of a cell was kept even so that no hydrostatic pressure arose from height difference. With no external pressure applied, any remaining miniscule pressure differences had negligible effect on current. The ion fluxes reported here were due exclusively to concentration differences and applied electric fields. The mechanics of how ion current flows through solution and nanopores is an important topic to discuss, before proceeding to the actual details of the experiment.

Ions and the solution that contains them are both in constant state of motion. Left alone, ions will equilibrate to a state where there is an equal distribution of ions throughout every corner of the solution, with constant movement of each individual ion. If a solution starts out with a concentration gradient entropy gradually forces mass movement of ions into the area with lower concentration. This phenomenon is referred

to as diffusion. Fick's Law describes the behavior of particles in a solution described before[41]. In one dimension it can be written, as:

$$J_{Diffusion} = -D\frac{dC(z,t)}{dz} \quad (2.2.1)$$

$J_{Diffusion}$ represents the diffusive flux of particles, D is the diffusion coefficient of the ions, and C is the concentration, as a function of z and t. It is necessary that the continuity equation, which is really an expression for conservation of mass, must remain fulfilled

$$\frac{dC(z,t)}{dt} = -D\frac{d\,J(z,t)}{dz} \quad (2.2.2)$$

We now substitute Fick's law directly into the right hand side of equation 2.2.2 and receive

$$\frac{dC(z,t)}{dt} = D\frac{d^2J(z,t)}{dz^2} \quad (2.2.3)$$

This is the diffusion equation in one dimension. Given sufficient boundary conditions and computing power, any system can be solved such that the final state and intermediate states can be recorded and analyzed. This equation also comes into play in reversal potential experiments, which are discussed later in this chapter.

Equally important is the force ions feel from electric fields. These fields are generated typically by inserting electrodes into the solution, and applying potential difference between them. Let us assume a particle has charge q, and the applied electric field is E. In the solution the particle will acquire a drift velocity, which is reached

when the electric field force is balanced by the drag force of the solution. The drift velocity becomes then a function of the applied electric field E, particle size $r_{particle}$, charge q, the fluid viscosity μ and temperature T. In order to estimate the drag force, we model the particle as a sphere, and use the Stokes formula

$$\xi_s = 6\pi\mu r_{particle} \tag{2.2.4}$$

to describe a term that will eventually represent the drag element. Using the notation above, the drift velocity is represented as

$$V_{Drift} = \frac{qE}{\xi_s} \tag{2.2.5}$$

which is the average speed an ion travels in the solution, given values for electric field and viscosity if the solution. We can also find an expression for the total ion flux. The total ion flux through an area is dependent on the concentration of ions locally, and the speed of ions through the area. Using the expression above for the speed, we receive the flux as a function of position and time in one dimension,

$$J_{electrophorsis} = \frac{qC(z,t)E(z,t)}{\xi_s} \tag{2.2.6}$$

an expression for the current due to the electric field, called electrophoresis. We can combine the terms for diffusion and electrophoresis to receive total current density.

$$J(z,t)_{Total} = \frac{qC(z,t)E(z,t)}{\xi_s} - D\frac{dC(z,t)}{dz} \tag{2.2.7}$$

Using Einstein's relation, where k_b is Bolztmann constant

$$D\xi_s = k_bT \tag{2.2.8}$$

we arrive at the relationship between current, concentration, and electric field known as the Nernst-Plank equation

$$J(z,t)_{Total} = D\frac{qC(z,t)E(z,t)}{k_bT} - D\frac{dC(z,t)}{dz} \quad (2.2.9)$$

an extremely useful tool in solving for current values using analytic software. Inside nanopores the electric field may be further complicated by the presence of surface charge. We, therefore, implement the Poisson equation,

$$\nabla^2 \emptyset = -\frac{\rho}{\varepsilon} \quad (2.2.10)$$

Here $\emptyset$ represents the potential with ρ and ε being the charge density and the permittivity of the solution, respectively. $\emptyset$ has a continuous first derivative everywhere except for at the pore walls, where

$$\frac{d\emptyset}{dr}|_{r=a} = \frac{2\sigma(a)}{\varepsilon}$$

This equation, in combination with the Nernst-Plank equation and boundary conditions, lay out a fully solvable ionic system which evolves in time. Computer software, such as MsPore, developed by Martin Burger, Maria Wolfram and Jan Pietschmann[10,11] and Comsol Inc. use continuum modeling to fully solve the Poisson-Nernst-Plank equation for our nanopores. Although this theory does not explicitly incorporate the finite size of ions or chemical ion-atom interactions with surface charge, PNP theory is an extremely useful tool for predicting ionic current inside nanopores.

Selectivity in nanopore systems is observed due to the surface charge and geometry of the cavity. Selectivity is defined as a preference for one ion over another due to size, charge, or chemical compatibility. Here we focus on charge induced selectivity. This is expressed as

$$S = \frac{I_+ - I_-}{I_+ + I_-} \qquad (2.2.11)$$

where I_+ and I_- represent the cationic and anionic currents, respectively. Highly selective devices are important scientifically, as often one is interested in only one species of ion. One way to measure selectivity is to take a reversal potential measurement[42,43,44]. Reversal potential is a voltage bias that can be measured, and whose value and sign give information about the polarity and strength of selectivity in a nanopore.

Pictorially the reversal potential can be seen in Figure 2.2.1. A conical nanopore is shown, but any cavity in which one opening is on the same order of the Debye length will show the same behavior. First, a concentration gradient is set up on both sides of the pore. Here, 100 mM KCl and 10 mM KCl have been chosen for our illustration. As discussed previously, ions on the left side of the membrane would diffuse to the right side due to the concentration difference if diffusion were the only driving force.

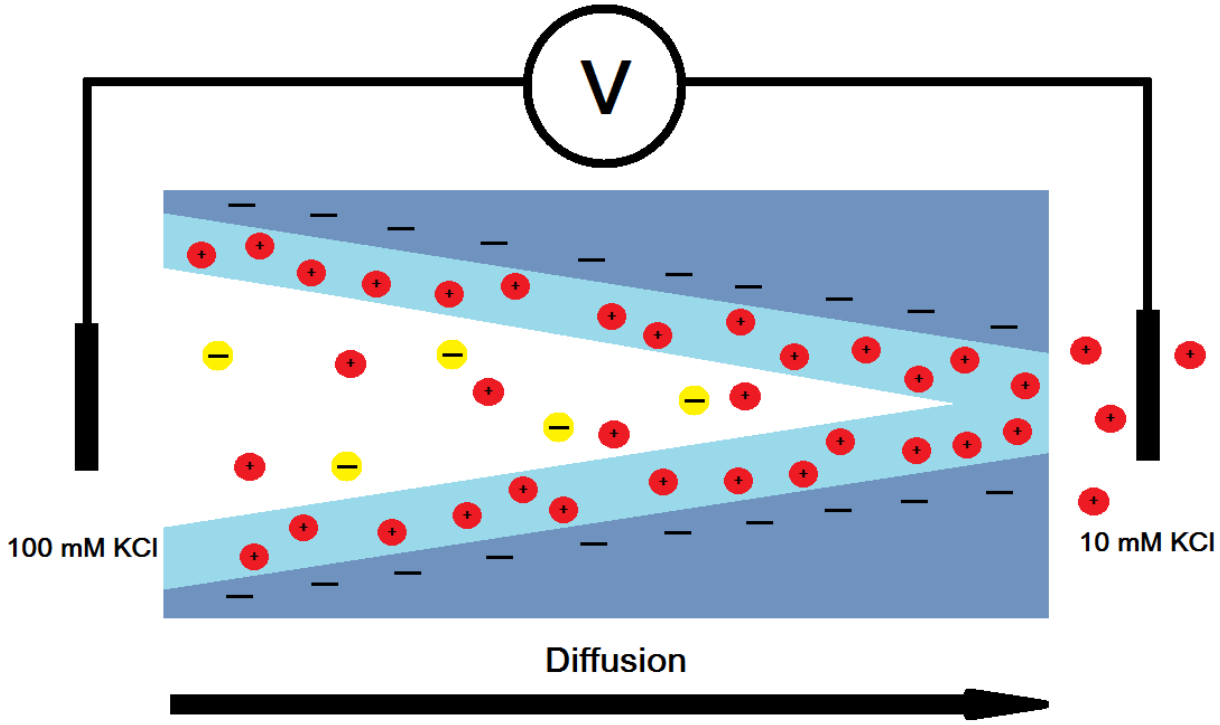

Figure 2.2.1 – A conical nanopore during reversal potential measurement. The left bulk concentration is 100 mM and the right 10 mM, setting up a tenfold concentration difference across the pore. Diffusion forces ions through the cation selective pore, setting up a charge build up on the right side of the pore. This creates a potential difference that can be measured.

However, the surface charge on the nanopore walls allows a much more dynamic and complex situation. As seen in Figure 2.2.1., the negative charge along the wall prohibits anion flow through the tip of the pore. Cation flow is uninhibited and diffusion pushes cations to the right side of the cell, through the membrane. This will not continue indefinitely. A charge buildup occurs due to the preferential flow of cations to the right reservoir, which then establishes a potential difference across the membrane, preventing ionic net flow. This difference can be measured by a potentiometer, or by taking a current-voltage measurement and noting the voltage at which zero current is recorded. This measurement is called the reversal potential.

The reversal potential is described mathematically by the Goldman-Hodgkin-Katz equation[45,46]

$$V_{reversal} = \frac{RT}{F} \ln \frac{x[K^+]_1 + [Cl^-]_2}{x[K^+]_2 + [Cl^-]_1} \quad (2.2.12)$$

where the value x is given by

$$x = \frac{D^K_{pore}}{D^{Cl}_{pore}} \quad (2.2.13)$$

The term $[K^+]_1$ represents the concentration of potassium in the left side of the cell and $[Cl^-]_2$ represents the concentration of chloride in the right side of the cell. The term *x* stands for the ratio of diffusion coefficients in the pore of the two considered ions. The reversal potential has a maximum theoretical value of ~57mV when the concentration on one side of the membrane is greater than the other by a factor of ten. Given a value for the measured reversal potential, one can solve for x using

$$x = \frac{[Cl^-]_1 \exp\left[\frac{V_{rev}F}{RT}\right] - [Cl^-]_2}{[K^+]_1 - [K^+]_2 \exp\left[\frac{V_{rev}F}{RT}\right]} \quad (2.2.14)$$

The value x is greater than 1 when the pore is selective for potassium ions.The considered analysis does not however take into account a possibility that ion concentrations in a pore can be voltage-dependent. Solving the Poisson-Nernst-Plank equations for a conical pore reveal that the concentration profile of ions inside the pore is indeed dependent on the voltage applied across the membrane, as seen in Figure 2.2.2. This profiles are not symmetric with respect to voltage, leading to a preferred direction of ion transport we call rectification[15].

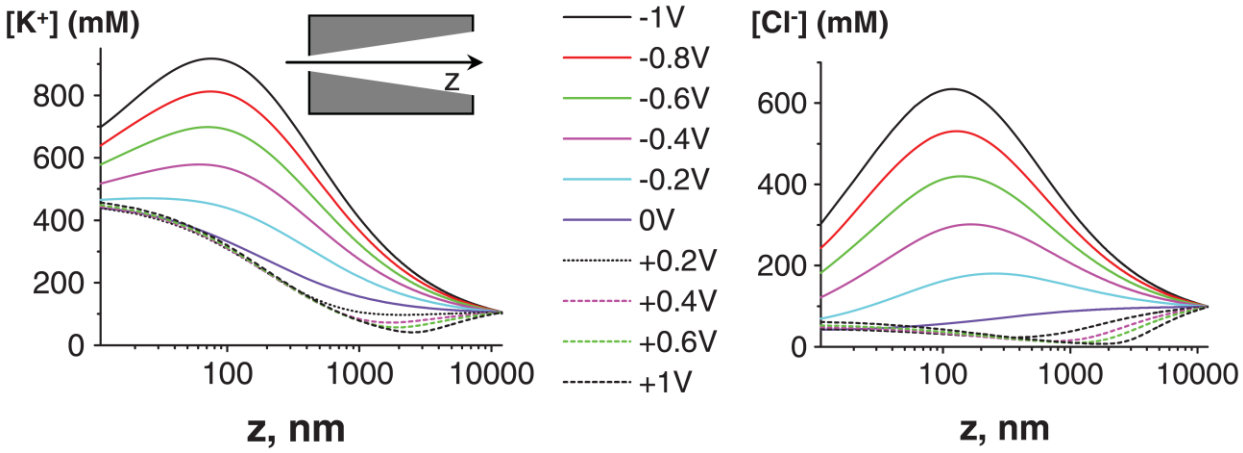

Figure 2.2.2 – COMSOL, Inc numerical calculations of potassium and chloride concentrations inside a conical nanopore, as a function of applied voltage across the pore, and distance along the pore axis. The surface charge was .5e / nm^2 and the pore dimensions were 5 nm and 500 nm for the tip and base diameter, respectively. The bulk concentration in this simulation was 100 mM, and the length of the pore was 12 micrometers. Reprinted with permission from reference [66].

Rectification is a transport property of our conical pores that results from surface charge, geometry, and applied voltage across the pore. Using the COMSOL modeling software, Poisson-Nernst-Planck equations were solved to get insight into ionic concentrations inside a pore with openings of 5 nm at the tip and 500 nm at the base (Figure 2.2.2). The surface charge was set to -0.5 e/nm^2. The modeling revealed that the tip of the pore had ion concentration higher than the 100 mM bulk value at any voltage. At forward bias (which is set as a negative voltage in our experimental setup), concentrations of both cations and anions increased with voltage to magnitudes above the bulk concentration. This voltage-induced enhancement of ionic concentrations leads to a nonlinear increase in current as larger negative voltages are applied. As a result, under forward bias the nanopore is only weakly cation selective. When we apply positive voltages (reverse bias), the current through the nanopore is limited by the

formation of a depletion zone. This zone of lower ion concentration, as seen in Fig. 2.2.3, increases in width as the magnitude of the reverse bias increases. The depletion zone also carries mostly cations; thus positive currents can be treated as cationic only. We define the rectification degree as the ratio of current recorded at positive and reverse bias at a set voltage magnitude.

The magnitude of the rectification ratio is both sensitive to the surface charge, the length of the pore, and the opening angle. Seen in Figure 2.2.3, continuum modeling MsSimPore predicts a peak of rectification as the surface charge is lowered, followed by a steep decline as the surface charge approaches zero[47].

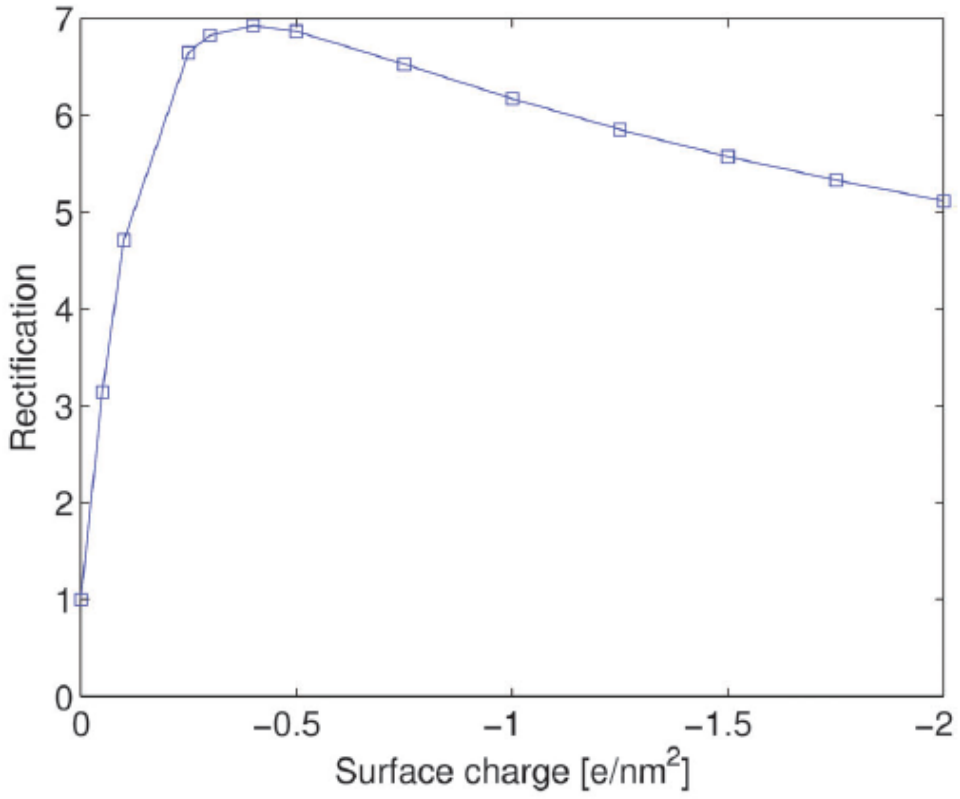

Figure 2.2.3 – Rectification as a function of surface charge density as predicted by the continuum modeled based on the Poisson – Nernst – Planck equations. The modeled nanopore had opening diameters of 6 nm and 812 nm, respectively. Rectification degrees were calculated as a ratio of currents at -1V and +1V in 100 mM KCl. Reprinted with permission from reference [47]

Thickness of the membrane which defines the pore length is also important when considering design of pores produced for rectification. Figure 2.2.4 shows a decay of rectification as the thickness of the membrane is decreased. In this simulation the tip diameter was 6 nm, and the cone angle was kept constant the length varied. The simulation was run in 100 mM KCl as the bulk electrolyte. This reduction in rectification manifested itself due to incomplete formation of the depletion zone when the membrane thickness is too small.

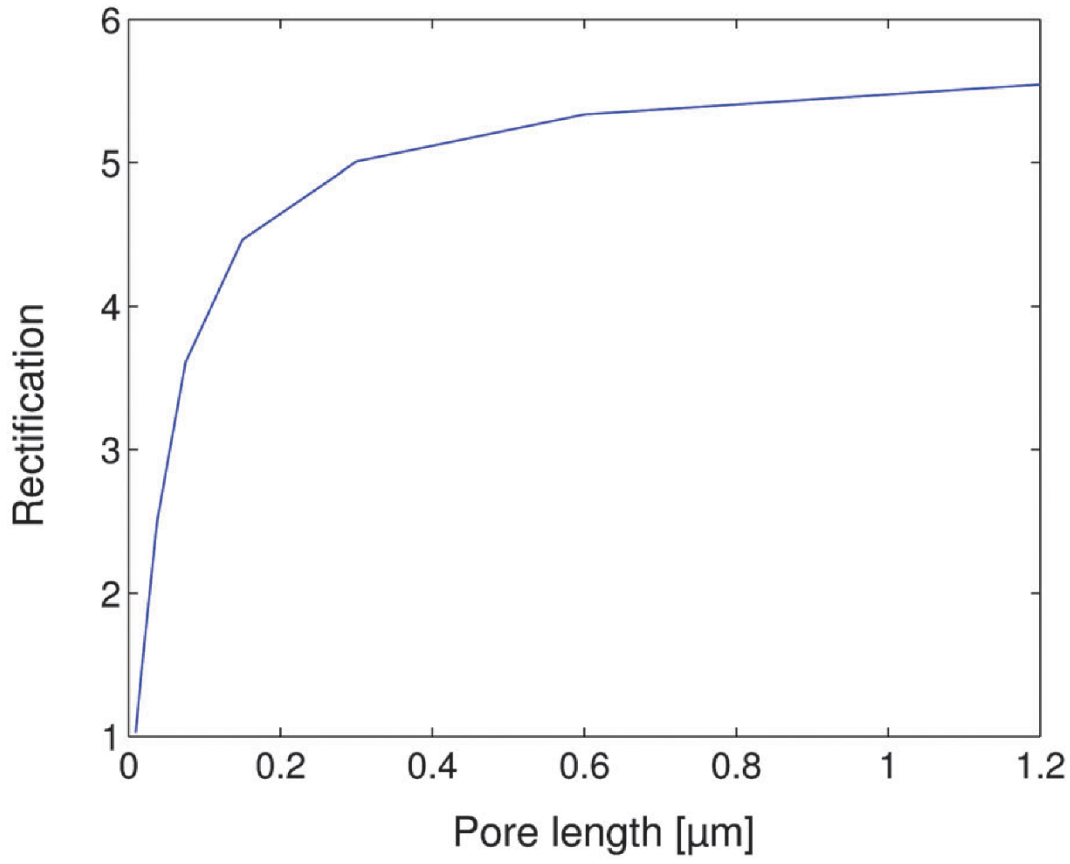

Figure 2.2.4 – Rectification as a function of length of pore. Each pore had a small opening of 6 nm, and the base opening was changed in order to keep the opening angle constant for every pore length. The voltage magnitude applied across the pore during rectification measurement was 1 V, and the bulk concentration was kept at 100 mM KCl. Reprinted with permission from reference [47]

In summary rectification of ion currents varies in magnitude depending on several parameters, yet the behavior is always seen in conical nanopores when the pH is above the isoelectric point of pH 3.8.

Now that the theoretical framework of ion current through nanopores has been discussed, the following chapters will focus on experiments completed using nanofluidic devices created with the methods discussed in Chapter 1.

Chapter 3

Study of lithium Ion Battery Material MnO_2 Using Cylindrical Nanopores

Maximizing the power output of electrochemical energy storage devices has been an ongoing goal for engineers and researchers worldwide. Next-generation supercapacitors are receiving increased attention as an energy solution. Valuable uses could be in modern electric cars for acceleration, or regenerative energy storage during breaking in Formula One race cars. These uses are ideal due to a supercapacitor's ability to produce large amounts of power per unit gram of active material. Making battery electrodes out of nanostructures is widely seen as an avenue to higher power at higher energy due to improved access of ions to energy storage electrodes[48,49,50]. The ion diffusion pathway is cut down significantly, leading to quicker charge and discharge reaction times, which is what researchers are attempting to optimize worldwide[51]. Outside energy and power output, stability during charge cycling has been a common concern with electrodes constructed from nano-architectures. Collecting knowledge about these processes, and the properties that allow them, is the goal of NEES (Nanostructures for Electrical Energy Storage) EFRC (Energy Frontier Research Center), which is a multi-regional national collaboration started in 2009 with federal government stimulus funds. Research centers are located at Yale, University of Maryland, University of Florida, Sandia National Lab, and University of California, Irvine. My project described below is in collaboration with Dr. San Bok Lee's group at the

University of Maryland. The goal set out for this project was to use electrochemical, non-destructive measurement techniques to characterize properties of the commonly used battery electrode material manganese oxide.

Manganese oxide is a popular energy storage material used in lithium ion batteries as well as supercapacitors. Previous studies[52] show it as an ideal material due to well understood electrochemistry, earth abundance, low cost, and relative ease in synthesizing. Our goal is to use nanostructures as test beds, to understand and characterize manganese oxide's properties and behavior. Specific surface area of electrodes can be measured by gas adsorption or estimated geometrically, however these approaches do not give information on whether the interior volume is fully accessible to ions during important electrochemical reactions. Single polymer cylindrical nanopores with an embedded manganese oxide rod created an experimental platform which is easily accessible, and can provide unique information on the properties of the porous material.

We present here a novel method of determining ion transport through the material manganese oxide. Our nanopores have the ability to probe multiple aspects of the material including surface charge, the electrochemical double layer, and interior pore size. Additionally a reversal potential measurement was made on manganese oxide to determine the sign of the surface charge, and to describe its selectivity. The measurement entails measuring a potential difference that is established across an ion selective membrane. Reversal potential measurements have been performed with polymer and biological channels previously. Here for the first time this method is applied to the porous inorganic structure manganese oxide, deposited inside a polyethylene

terephthalate (PET) nanopore in the form of a several hundred nm diameter cylindrical rod.

3.1 Preparation and Characterization of MnO_2 Rods

Multipore samples were first used to optimize the deposition of manganese rods into the nanopores. The rods need to stay connected electrically during the entire deposition to give consistent lengths as well as to guarantee a complete filling of the entire cross-section of the pore. This is important, because any gap between the manganese oxide rod and the polymer surface would lead to measurement of the conductivity of the gap, and not the rod. The rod's ionic conductance was expected to be much lower compared to the conductance of an empty pore. Multipore samples are beneficial due to the high volume of rods that can be grown and tested simultaneously. In the case of deposition failure, the type of failure and chance of such an error occurring in the future can be easily identified.

First established by the University of Maryland graduate student Eleanor Gillette was a relationship between deposition time and rod length. This relationship is used later to report the rod length of samples in our research. AAO (anodic aluminum oxide) was used as the multipore template due to difficulty in dissolving PET without simultaneously dissolving the enclosed manganese oxide rods. AAO polymer matrix can indeed be easily dissolved in 3M NaOH without harming manganese oxide rods to be later characterized. The AAO multipore membranes used in the research were

purchased from Whatman. The samples had 200 nm in diameter cylindrical pores at a density of 10^9 pores/cm[52]. Properties of rods grown in AAO, polycarbonate, and PET membranes should be identical since the growth occurs at the gold – solution interface, and is expected to be independent of the template. Deposition of rods was performed in 100 mM aqueous solution of manganese acetate. The active species in this solution were the manganese ions, which were oxidized from a 2+ state to a 4+ state when combining with oxygen to form manganese oxide. A 200 nm thick gold layer was sputtered onto one side of the membrane. This provided both an outside electrical contact as well as a surface for the manganese oxide rod to grow from. The gold layer did not close the pore entirely; rather it coated the inside of the pore just enough for the manganese ions in the solution to have a reactive surface when the potential was applied, as seen in Figure 3.1.1. The deposition was performed at 0.6V vs Ag/AgCl. Voltages up to 1.2V can be used for the deposition,

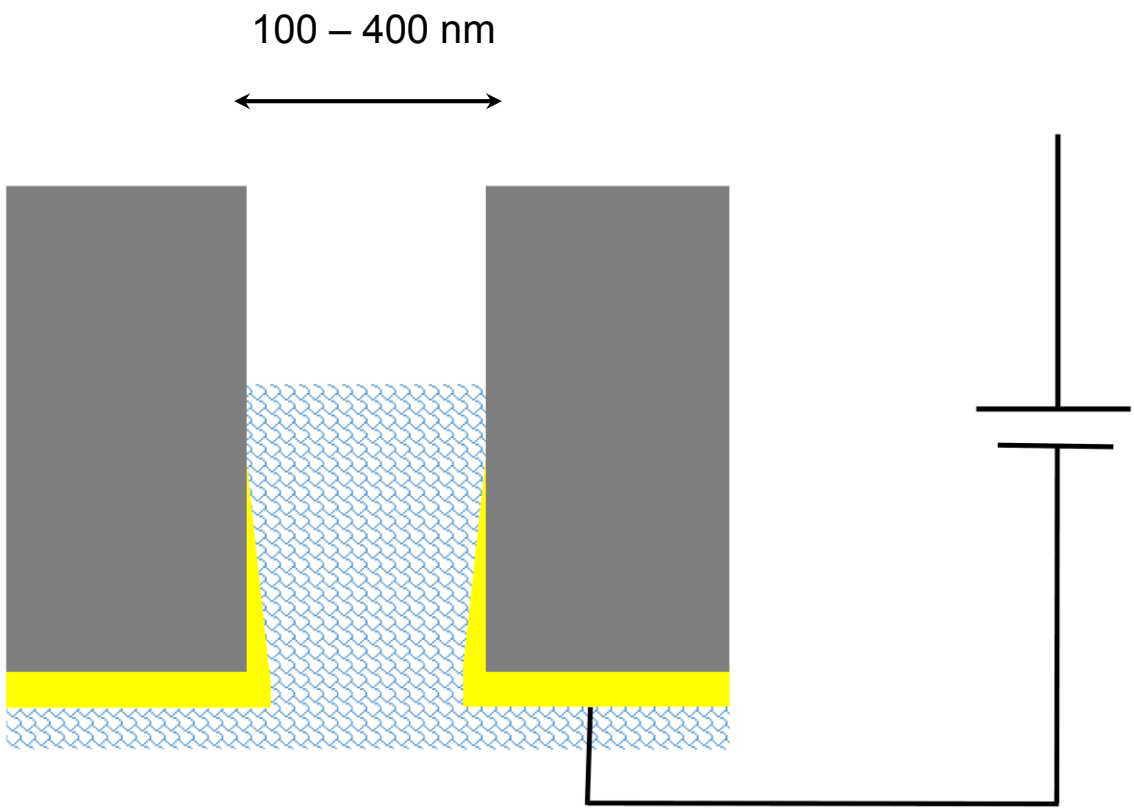

Figure 3.1.1 – Diagram of manganese oxide growth inside PET nanopore. 200 nm gold layer allowed direct electrical connection for application of 0.6V deposition potential.

however, lower voltage allows for a slower deposition and filling the entire whole cross-section of the pores[53]. Once the rods were grown, the gold was removed, followed by dissolving the AAO template. Sonication was then used to separate the rods from fragments of AAO that may not have fully dissolved. The solution was then dried out on top of SEM safe carbon tape. For conductivity and contrast during SEM imaging a 10

nm gold layer was deposited on top of the sample. As seen in Figure 3.1.2, the length of the rods was not entirely uniform for a set deposition time. An average deposition time versus rate of the length increase as well as a standard deviation was therefore calculated.

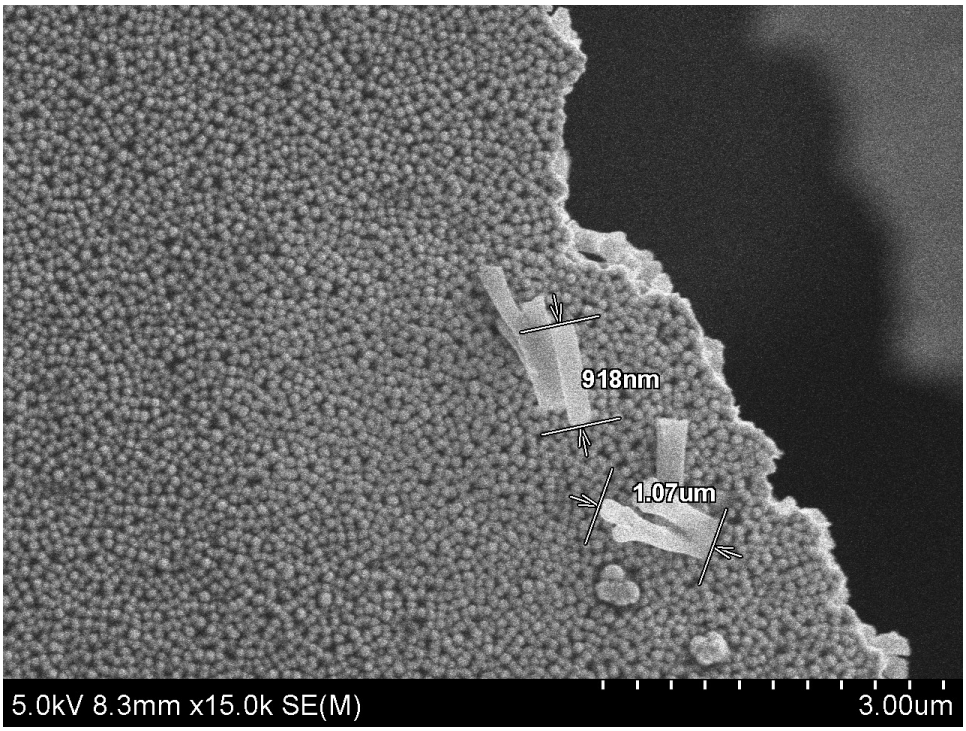

Figure 3.1.2 – Free manganese oxide rods imaged with SEM. The wires sit atop an island of manganese oxide leftover after the AAO template was dissolved. The rate for deposition length verses time was calculated by averaging rod lengths in each sample, then comparing sample averages.

Figure 3.1.3 shows the deposition rate was determined to be 250 nm / minute with a standard deviation of 35 nm / minute. These rates, gathered from multipore samples, were used to estimate rod length for the single pore experiments.

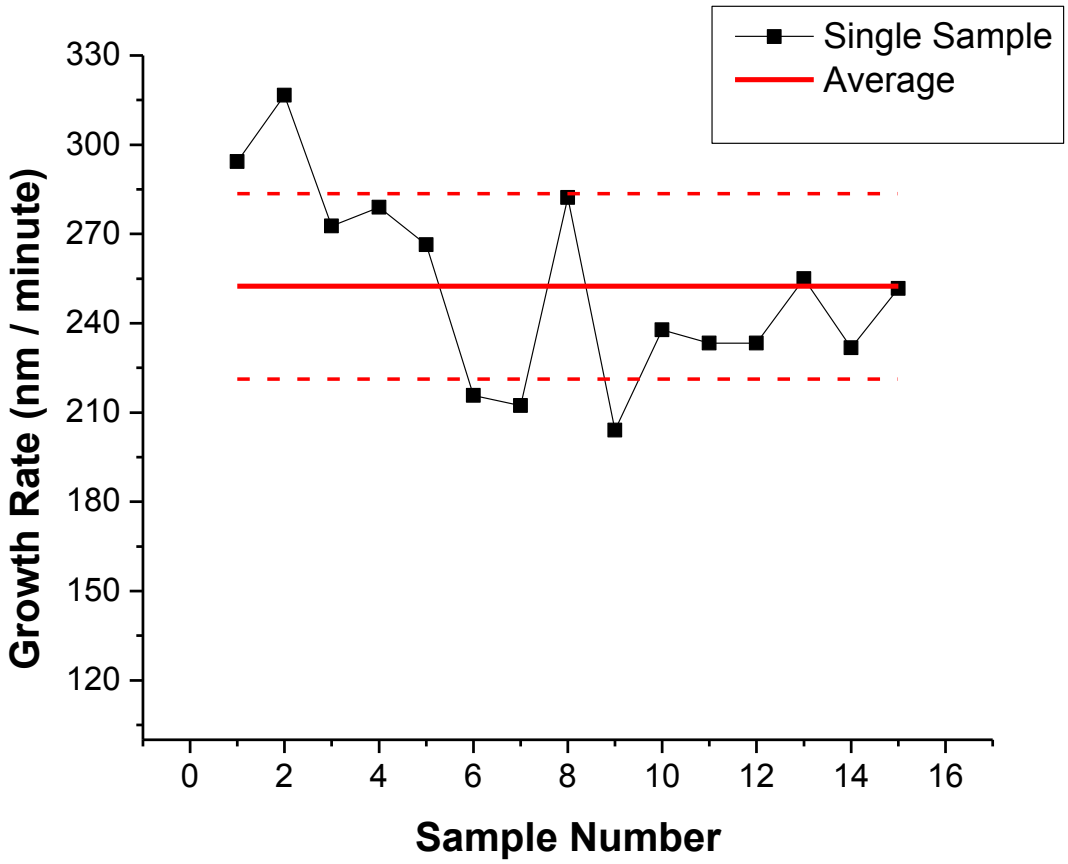

Figure 3.1.3 – Rod growth rate across 15 manganese oxide multipore samples (black) and average growth rate (red). Standard deviation is shown as the dotted lines above and below the average growth rate. Samples 1-7 were grown using electrodeposition for 3 minutes, while samples 8 -10 were grown for 4.5 minutes, and samples 11-15 for 6 minutes. The average growth rates for the groups were 285, 241, and 251 nm/minute, respectively. Average length of rods in each sample was gathered from SEM images taken after the template was dissolved.

[51]The final images of the wires can be seen in Figure 3.1.4. SAED (Small Angle Electron Diffraction) shows the amorphous structure of the material. The absence of discrete rings is evidence that the electrons did not have any consistent atomic spacing to diffract off of when passing through the material. Instead seen is a continuous ring of varying intensity, typical of a material with random interior spacing. Also shown is a

TEM (Transmission Electron Microscope) image of multiple wires. It depicts a darker manganese oxide core with a thin layer of AAO substrate that did not fully etch away. Preparation and characterization of the manganese oxide wires was a systematic and collaborative effort. Confidence in the process lends certainty to future experiments.

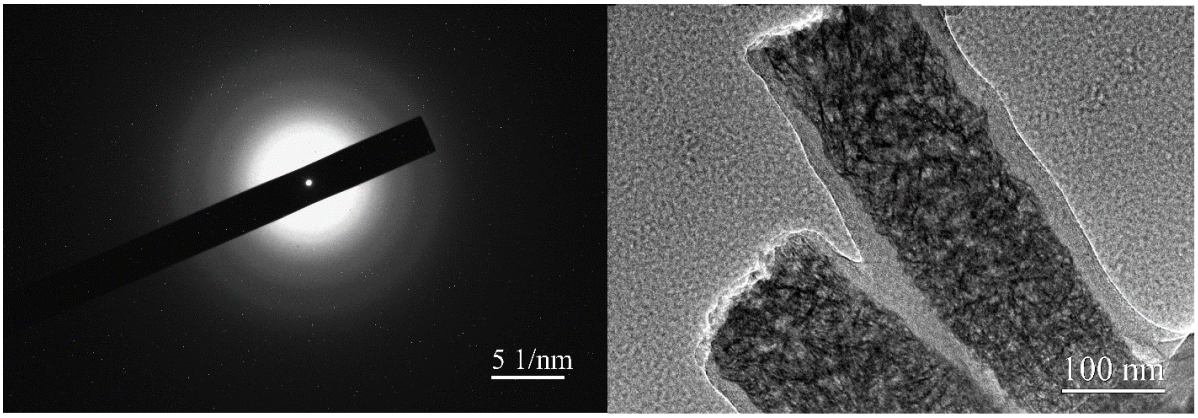

Figure 3.1.4 – (a) Small Angle Electron Diffraction of manganese oxide rods deposited in a polycarbonate template taken with Transmission Electron Microscope (TEM). Lack of rings suggests amorphous structure of manganese oxide. (b) TEM images of manganese oxide rods after dissolving the polymer template. The thin layer on the rods is most probably an undissolved AAO.

3.2 Experimental Techniques and Results on Electrochemical Characterization of Single MnO_2 Rods.

In order to investigate transport properties of voids in manganese oxide, single pore samples with embedded manganese oxide rods were prepared. Depicted in Figure 3.2.1 is a scheme of our experimental setup. Two non – polarizable Ag/AgCl electrodes, one on each side of the membrane, were used to generate an electric field while

simultaneously measuring the resulting ionic current across the pore. A maximum magnitude of three volts replaced the range of five volts that was used when measuring empty nanopores. High voltages were found to make the transport properties of the rods unstable. The time frame in which experiments were performed was much less than manganese oxide's known lifespan when immersed in water.

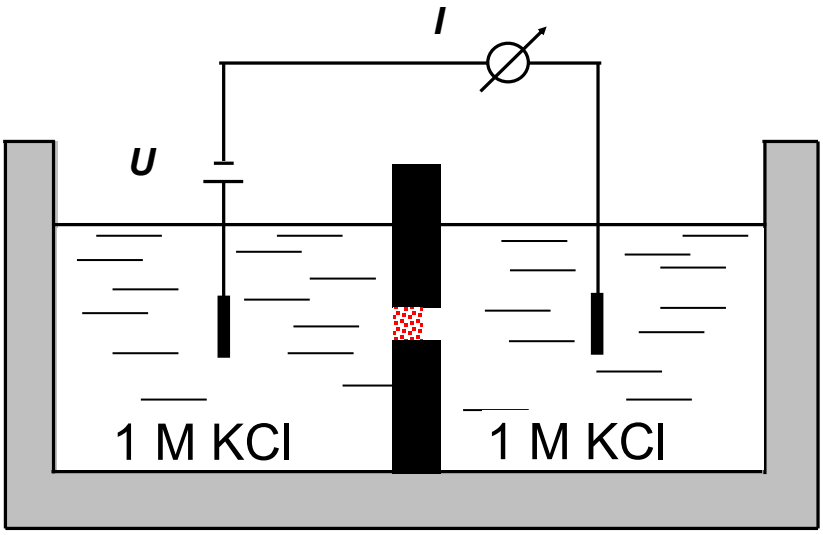

Figure 3.2.1 – Scheme of embedded manganese oxide rod during setup during current – voltage measurements. Voltage is applied across the membrane by symmetric electrodes, causing current through the rod, which is then recorded with Keithley 6489 picoammeter.

Manganese oxide decay in aqueous solution even without any applied potential was previously discovered[51,52]. Irreversible reactions that take place in aqueous solution result in manganese oxide's soluble forms, such as Mn_2O_3 and Mn_2O_7. Influence of the decay was avoided by performing a complete series of experiments on the same day when possible, or drying out the cell when not in use. Control runs of 1M KCl were used

to verify that samples were performing similarly and consistently across days for prolonged experiments.

First, empty nanopores were characterized before deposition. Pore opening was estimated based on a current – voltage curve recorded in 1 M KCl. In addition, current – voltage curves for a wide range of KCl concentrations was recorded as well. These currents were recorded for the purpose of comparing transport properties measured before and after manganese oxide is deposited. In most cases the current after deposition was significantly lowered.There were few samples for which the attempted deposition did not result in any change of the current. We suspect these samples did not have deposited manganese oxide, or the rod fell out during shipping, or the rod fell out when voltage was applied during current measurements. Thus these samples were not further investigated. Figure 3.2.2 shows example current-voltage curves before and after deposition of MnO_2 in two different, single-pore membranes. Significant lowering of the currents after MnO_2 deposition suggests the rod was indeed present in the pore increasing the system resistance.

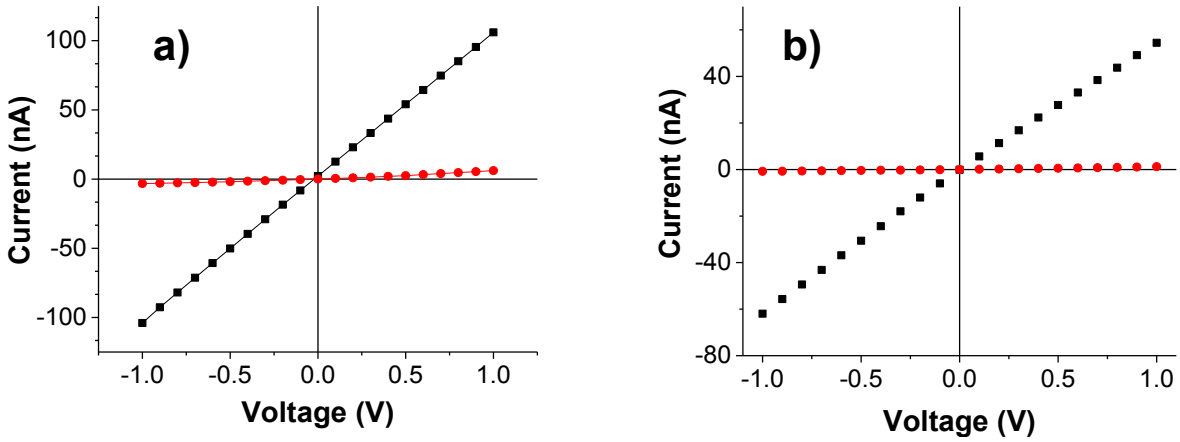

Figure 3.2.2 – Comparison of current through single cylindrical nanopores before and after manganese oxide deposition. Black circles representing current before deposition; red circles representing current after deposition. The opening diameter of the pores before deposition was (a) 374 nm, and (b) 304 nm.

Finite currents through the rods however suggest the structure is porous. Another striking property was saturation of ion currents for KCl concentrations below 100 mM, observed in the systems with MnO_2 (Figure 3.2.3) . Thus, even though the electrolyte concentration was lowered from 100 mM to 1 mM, the observed currents remained almost the same. This saturation of ion currents was independent of the diameter of the pore in which the MnO_2 deposition was performed, and occurred between 50 mM and 100 mM KCl. In contrast, an empty nanopore did not exhibit the saturation, and the current decreased with the decrease of KCl concentration. A display of this saturation behavior can be seen in Figure 3.2.3. Shown are currents of an empty pore and pores with manganese oxide embedded. Below we discuss the origin of the current saturation, and explain how this effect can be used to estimate effective pore opening of the voids[52].

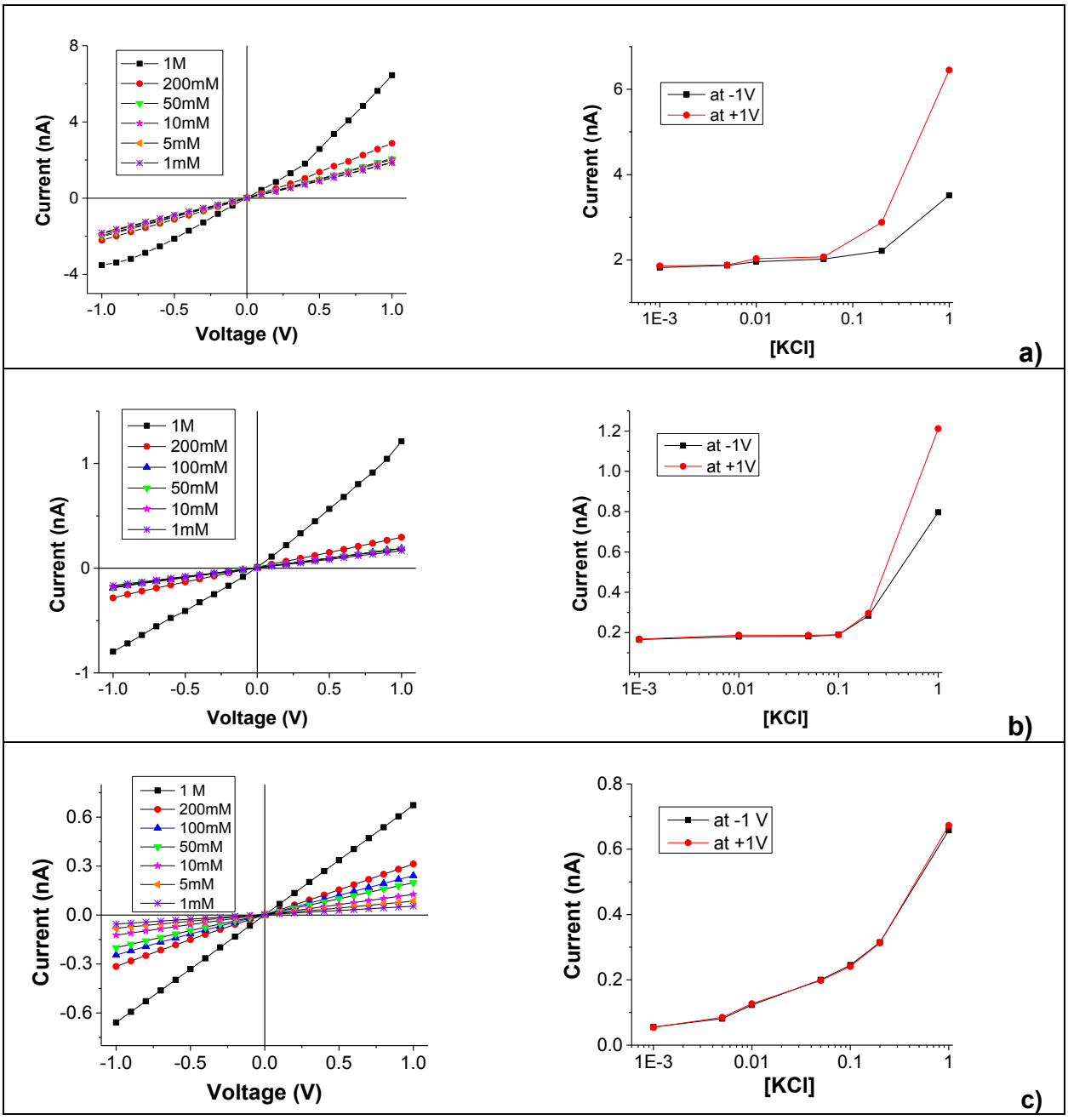

Figure 3.2.3 – Left panels show current – voltage recorded through cylindrical nanopores. Right panels show current magnitudes at +1 and -1V, as a function of KCl concentration. (a) And (b) represent pores with 200 nm long manganese oxide rods deposited inside, with pore diameter of 374 nm and 304 nm, respectively. (c) Empty cylindrical nanopore with diameter of 50 nm. Saturation is not seen at low concentration in the empty nanopore. All solutions were buffered to pH 8, and values represent averages over three independent voltage scans.

Manganese oxide is known to have a negative surface charge in aqueous solution. This is due to an effect called “charge determining ions”[54]. In short, a surface in solution has a finite affinity towards ions and molecules in a solution. A well-known example is the case of gold in an aqueous solution containing chloride ions. The gold, in KCl solution for example, will become negatively charged due to adsorption of chloride ions. The situation in our experiment is similar to the gold example. Hydroxide has a large affinity to MnO_2 surface rendering it negatively charged down to pH of 2.4, where the surface becomes overall neutral. At pH 2.4, hydronium ions are believed to start adsorbing strongly. At these conditions the slow background electrochemistry that breaks down and dissolves manganese oxide becomes greatly accelerated. Any experiments done at such a low pH will fail due to rapid deterioration of the material. We conservatively performed all experiments at the pH range between range 4 and 8. We preformed measurements at pH 4 to confirm that the recorded current was not dominated by hydronium ions passing through the rods. We recorded currents at 1V at pH 4 and 8 for KCl and LiCl, both at 1 mM concentration. The four order of magnitude increase of hydronium ions decreased the recorded current by ~15%. The small current change with the four unit pH change also shows that the current recorded is through the manganese oxide wire and not a gap between the wire and the PET surface. pH 4 is however near the isoelectric point of PET, and a current decrease of a factor of at least a factor of 2 was previously seen with empty PET pores when changing pH from pH 8 to pH 4. Manganese oxide maintained negative surface charge at both pH 8 and pH 4 thus the currents at these two pH values are comparable.

The Debye double layer, always formed near charged surfaces in solution, can be used as tool to probe geometrical and electrochemical properties of nanopores and nanovoids. Here we apply this tool to get an estimate for the void size in manganese oxide structures such as the rods we deposited. The double layer thickness can be approximated by

$$\lambda = \frac{0.3\ nm}{\sqrt{C_0}} \qquad (3.2.1)$$

as explained in Chapter 2. Inside the confined space of a nanopore the conductivity of the pore, and ionic concentrations in the pore, will be influenced by the presence of surface charges. That fact allows us to use the ion current to infer information about the double layer as well as effective opening diameter of the voids. The excess ion concentration inside the double layer is determined by the surface charge. If the molarity of the bulk solution is lowered significantly, the ion concentration near the double layer becomes independent of the bulk and determined only by electroneutrality. Thus, if the pore radius is comparable to the thickness of the double layer, the pore will exhibit ion current that is independent of the bulk concentration. Seen in Figure 3.2.3, saturation of ion currents in the system of manganese oxide suggests that the voids are completely filled with electrical double-layer. Figure 3.2.3 shows the results for several samples, along with an empty cylindrical nanopore. The 50 nm empty nanopore does not show saturation at low KCl concentration, further strengthening our conclusion. Since the saturation point was ~50 mM, using Equation 3.2.1 we obtain a double layer/void radius of ~3 nm. It is important to underscore the significance of this series of experiments. This is the first estimation of the effective opening of voids in MnO_2 which

are accessible to ions. This is also the first demonstration of the existence of a connected network of pores and direct evidence of high porosity of MnO_2.

Existence of the ion current saturation confirms presence of surface charges. However, it does not reveal the polarity or selectivity of the material. Reversal potential measurement, as used before for biological and man-made nanopores, was therefore performed. The set up for this experiment is seen in Figure 3.2.4. Briefly, the measurements entail recording potential difference that is created across a membrane in contact with a salt concentration gradient. At room temperature, and at ten times concentration gradient of 1:1 electrolyte, e.g. KCl, a perfectly anion or cation selective membrane would cause formation of a 59 mV Nernst potential. For less selective membranes, the values are lower; non-selective membranes do not establish any measurable potential difference in KCl. Plain rod Ag/AgCl electrodes could not be used for the measurement since the electrode potential is dependent on the KCl concentration, and the measurement requires salt gradient. For the Ag/AgCl electrode immersed in KCl solution where a reduction is taking place, the electrode's potential is given by

$$E_{reduction} = E^0 + \frac{RT}{zF}\ln[Cl^-] \qquad (3.2.2)$$

where E^0 represents the standard potential of Ag/AgCl. In a full cell configuration and symmetric electrodes (and non-symmetric concentrations) the theoretical cell potential becomes

$$E_{Cell} = E^0_{cell} - \frac{RT}{zF}\ln[Q] \quad (3.2.3)$$

where E^0_{cell} becomes zero since the electrodes are identical. Q represents the reaction quotient, and is given by

$$\frac{[Cl^-_1]}{[Cl^-_2]} \quad (3.2.4)$$

thus the ratio of concentrations on either side of the pore. As can be seen if one uses symmetric electrodes and equal salt concentrations on each side of the cell, no intrinsic potential difference will be created. With a cell set up such that side one has 100 mM and side two has 10 mM the cell bias will be 59 mV. This is a large value, and washes out any reversal potential value that we try to measure. In the measurements of reversal potential, Ag/AgCl electrodes with salt bridges are typically used. Following a standard recipe reported below, we made gel electrodes to fulfill the purpose of recording reversal potential measurements accurately. Figure 3.2.5 shows a scheme of the electrode. The electrodes were made with 1 mL pipette tips, Ag/AgCl electrode rods, and rubber stops to seal the openings. This design is such that the Ag/AgCl electrode rods are in contact with 3 M KCl in the pipette tip; no potential difference builds up between the rods due to the above mentioned Nernst potential. The high concentration also guarantees that within the course of the experiment the KCl concentration inside the pipette tip will remain constant. Agar gel is used to prevent mixing of solution inside the pipette tip with solution inside the cell during experiment. It has the dual purpose of allowing current to flow from the cell to the electrode inside the pipette tip. The agar gel is made by mixing 100 mL of 3M KCl solution with 3 g agar powder. This mixture is brought to a boil under constant stirring until it thickens. 200mL of the solution is sucked

into the pipette tip and left to cool. Because of the presence of high concentration of potassium and chloride in the agar, the gel easily passes current from the cell solution to the electrodes inside the pipette tip. The high molarity of KCl in the gel allows ions at the surface of the gel to carry a high fraction of the current, which lowers the need for ions to diffuse through the entire length of gel, reducing junction potential. These electrodes showed accuracy of ~1mV during repeated scans.

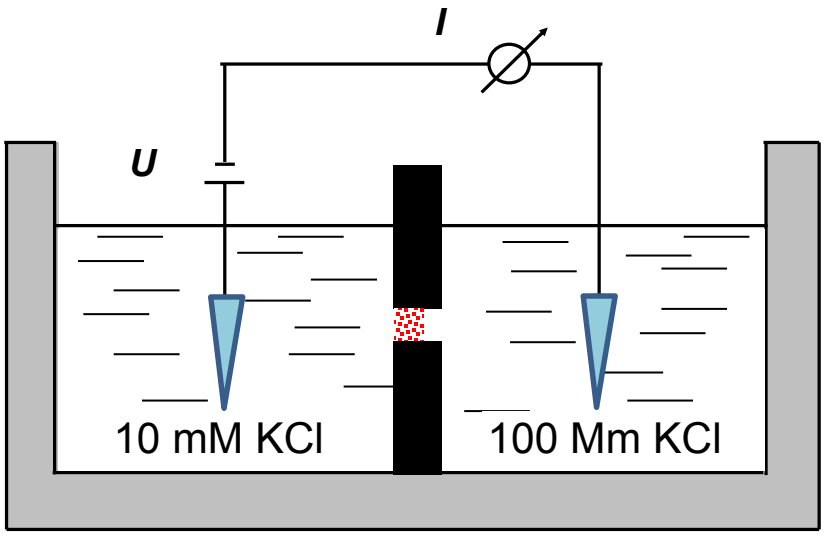

Figure 3.2.4 – Cell set up for reversal potential measurements. Homemade KCl – gel electrodes are used to isolate the electrodes form the solution, eliminating Nernst potential interference.

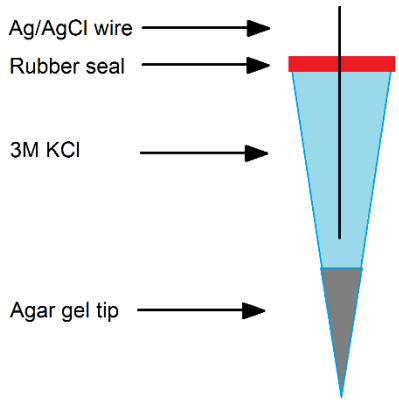

Figure 3.2.5. – Diagram of gel electrode used for reversal potential measurement. Agar tip was made with water at 3M KCl concentration to provide conductivity during measurement.

Figure 3.2.4 shows the membrane oriented such that the manganese oxide rod is on the left side of the cell. The gel tipped electrodes are placed on both sides, after test runs measuring and confirming the lack of significant potential difference between them. The gel electrodes had a small stable potential difference between 1 and 5 mV. This was due to imperfections in their construction, possibly differences in earlier deposited AgCl. The small potential difference was subtracted out of any final measurements. Figure 3.2.6 shows an example measurement of the reversal potential, on a pore with original opening diameter of 270 nm and deposited manganese oxide. The measurement was performed by recording current – voltage curves in the range between -150 mV to +150 mV using 2 mV steps. Presence of a finite reversal potential can be observed as a non-zero current at 0 V; value of the reversal potential is equal to the voltage for which the transmembrane current becomes zero. In the case when the MnO_2 rod was in contact with a lower concentration of 10 mM KCl, the reversal potential was 40 mV. From Goldman – Katz equation (equation 2.2.12), one can then calculate

the ratio of diffusion coefficients of K and Cl in the pore to be 10. When the salt gradient was reversed, the reversal potential was lower and equal to 30 mV, with a calculated ratio of 5. The results indicate, the manganese oxide rod was cation selective regardless of orientation, with higher selectivity when the rod was in contact with the lower molarity solution. This is consistent with the electrical-double layer properties as the solution molarity affects the double layer length. This in turn affects the selectivity of the embedded manganese oxide wire. Higher concentration shrinks the double layer, rendering the manganese oxide less selective for potassium ions, lowering measured reversal potential. Reversal potential measurements were also performed in LiCl due to importance of the salt for batteries used in EFRC collaboration. Cation selectivity of the voids in LiCl was confirmed.

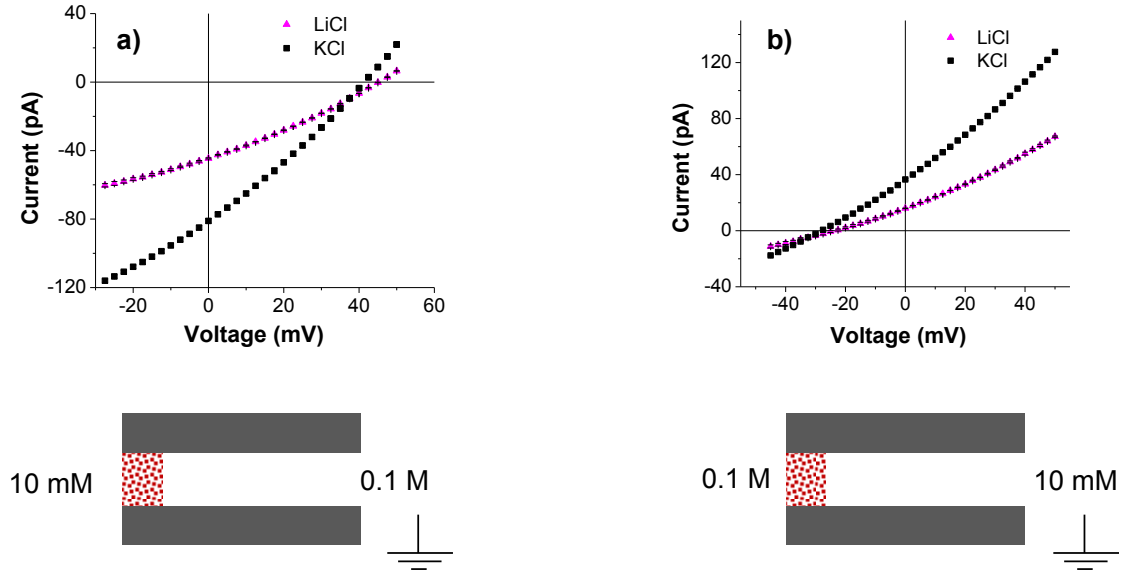

Figure 3.2.6 – Reversal potential measurements for 270 nm single cylindrical pore with manganese oxide deposited. KCl (black) and LiCl (magenta) represent currents when the manganese oxide is in contact with the lower (a) and higher (b) concentration. Average of three independent scans is shown.

Expansion on the idea of using cylindrical nanopores to test manganese oxide has already begun. An interesting and novel idea is to compare properties such as ion conductivity, surface charge, and void size of manganese oxide with its reduced form. When reduced, manganese valence goes from +4 to +3. The chemical formula shifts from MnO_2 to MnOOLi or MnOOH. Literature suggests that in aqueous solution hydrogen is the cation that primarily responsible for reduction. This is due to higher mobility of hydrogen and possibly a faster intercalation process compared to lithium ions. With the manganese oxide rod inserted into the nanopore in such a way that there is an electrical connection from the rod to an outside source, we can reduce the rod and measure in situ properties such as conductance, void size, and surface charge.

First set of experiments was performed with polycarbonate membranes containing many pores with density of 10^8 pores/cm^2. Membranes used in the measurements had an average opening diameter of 200 nm. A gold layer was sputtered on one side of the membrane using a Denton Desk 4 vacuum sputter to a thickness that matches 25% the diameter of the pore. The gold layer also covered the back of the PET film. This allowed for an easy electrical access to the inside gold layer that touches the metal oxide. CH Instruments Model CHI650C Electrochemical Analyzer was used to apply a negative potential to the copper tape which was electrically attached to the gold layer. First experimental results shown in Figure 3.2.7 suggest, reduction of the rods diminishes their ionic resistance. This measurements can be interpreted via reduction induced increase in void size, which would match the previous studies on manganese oxide swelling during charging[51].

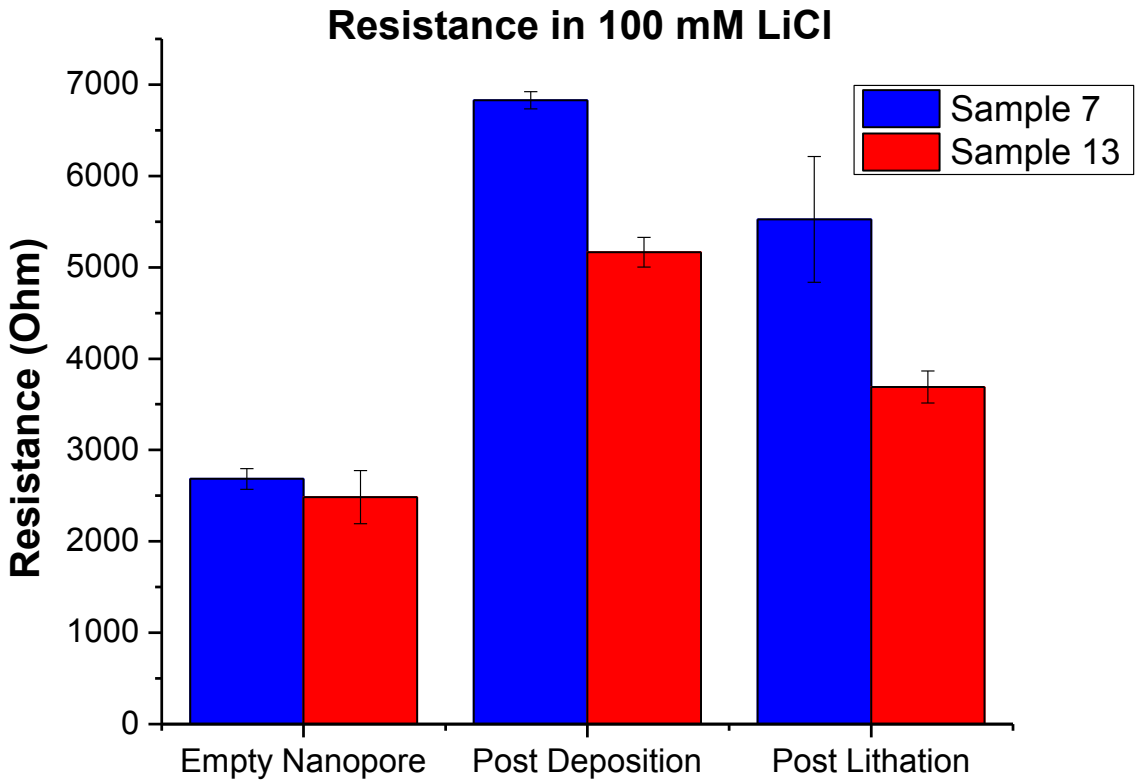

Figure 3.2.7 – Resistance measurements of multipore 200 nm cylindrical nanopores with manganese oxide nanorods deposited. Resistance after deposition of MnO2 is lowered by the intercalation of lithium ions when held at negative potential.

Through the use of cylindrical nanopores and electrochemical measurements, we have succeeded in measuring properties of manganese oxide relevant to the EFRC collaboration. We found conclusive evidence that current can flow through manganese oxide for lengths up to 1500 nm. Current saturation at low molarities was observed at 50 mM, pointing to void sizes under 5 nm in diameter. As manganese oxide is known to swell and compress during charge cycling, it will be a future study to examine how this void size changes during the cycling steps. We sought and achieved confirmation of

negative surface charge of manganese oxide in aqueous solution. Our reversal potential approach probed surface charge of ion accessible voids, which cannot be investigated using the zero point of charge method.

Chapter 4

Lithium and Other Alkali Metal Binding to Surface Charges

Many nanoscale devices such as ionic circuits, artificial ion selective membranes, and nano-transistors depend on homogeneous and sometimes complex surface charge patterns to function. Modulation of these patterns will have large implications on the functionality of these devices. We seek to study surface charge modulation inside PET nanopores, as they are the building blocks for nanofluidic devices prepared in our laboratory. We also focus on lithium, as that is the ion commonly used in battery applications. Charged species will have an affinity towards surfaces, however large or small. This is dependent on electronic orbital interactions between the ion and the surface. The surface may be similar to manganese oxide and develop a surface charge that is due to a preferential affinity towards hydroxide ions. The surface may also have a permanent surface charge due to a previous chemical reaction, an example being PET surface after sodium hydroxide etching. In this chapter the surface charge is not caused by a “charge determining ion” such as hydronium or hydroxide. Our surface charge is due to cleaving of ester bonds on the PET chains, leaving exposed carboxyl groups. We choose to study the interaction of carboxyl groups with various alkali metals: lithium, potassium, and sodium. The motivation for this study comes from an interest in lithium’s interactions with the battery electrode material manganese oxide, a charged surface that lithium interacts with during cycling. Questions about lithium’s interactions with

architectures on the nanoscale can be answered by using conical PET nanopores as a test bed. Conical nanopores have nano – constrictions with surface charges on the walls, which are similar to the voids found in manganese oxide.

4.1 Affinity of Ions to Surface Charges

An ion's tendency to stay near a surface is due to polarity and magnitude of the surface charge density as well as the ion's charge. Multivalent ions have been observed to oversaturate charged surfaces, leading to charge inversion[11], so that originally negatively charged surface became effectively positive. Rectification, i.e. the effect when currents for one polarity are higher compared to the currents recorded for the corresponding voltages of the opposite polarity, has been found to depend on the pore opening diameter, pore geometry, and distribution of surface charges on the pore walls[55–60,47]. Rectification properties of single conically shaped nanopores in electrolytes containing multiple charged cations differed from the properties measured in KCl[61]. The goal of our study was to check for differentiating behavior of rectifying nanopores within singly charged ions of lithium, sodium, and potassium. When in water, each ion acquires water shell, lithium having a radius of 300 pm, followed by sodium at 225 pm and potassium at 150 pm[62]. Aside from size difference, the ions have different chemical affinities towards charged groups, as shown recently with carboxyl groups in the α-hemolysin pore[63]. As a consequence, ions can differ by the average time they spent in the vicinity of a carboxyl (or another charged) group. Some ions chemically adsorb onto the surface while some ions stay nearby the surface due to the potential well

caused by charged groups. This was seen previously in the above mentioned study of the α-hemolysin pore performed using molecular dynamics approach. In the model, the pore was filled with LiCl, NaCl, KCl, RbCl, and CsCl salts at neutral pH. An electric field was applied across the membrane, and the resulting surface charge and ion current were modeled. Although α-hemolysin is weakly anion selective, it does have 63 negatively charged carboxyl groups along the surface exposed to the pore lumen. Ion current passing through the α-hemolysin pore is also rectified, thus the α-hemolysin molecular dynamics modeling results are very relevant for understanding interactions of alkali salt ions with carboxyl groups inside our PET nanopores.

Experimentally measured transport properties of the α-hemolysin pore were also reported and revealed the lowest currents and rectification degrees in LiCl[63]. One theory for these observations was based on size exclusion due to the increased size of a hydrated lithium ion compared to the other ions tested. A scheme of this with hydrated values can be seen in Figure 4.1.1

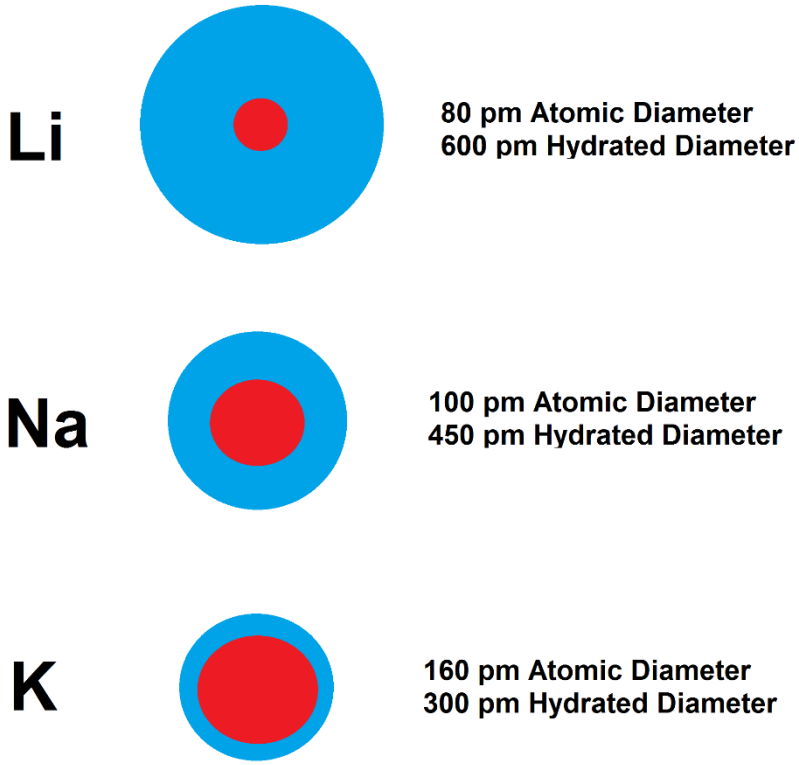

Figure 4.1.1 – Atomic and hydrated diameters of selected alkali atoms. Red represents the atomic size, blue represents the hydration shell.

Modeling of the α-hemolysin pore revealed binding of all studied monovalent ions to the carboxyl groups, with lithium having the largest affinity and spending the longest time near the surface charges. Lithium and sodium ions that interacted with a carboxyl group had a binding time that was longer than the time it took on average for a lithium ion to transit the length of the pore. Potassium, rubidium, and cesium all had a binding time that was smaller than their transit time. As a result, lithium and sodium were most effective at causing a partial neutralization of the surface charge. In our study we tested

whether these monovalent ions can modulate surface charge of our PET nanopores as well. This study is very important in assessing which interactions of ions with surfaces are important for qualitative and quantitative understanding of ionic transport at the nanoscale. This knowledge can then be used to design effective and efficient nano – architectures for future supercapacitor and battery electrodes.

4.2 **Setup: Experiment and Modeling**

Conical nanopores used in this study were fabricated and characterized as described in chapter 1, and had an opening diameter between 3 and 25 nm. The large opening of the pores was between 300 and 750 nm in diameter as seen in Figure 4.2.1. The pores were then tested in aqueous salts with range of concentration 10mM to 200mM. Current-voltage curves were recorded in the following order. We stared with experiments in KCl, followed by measurements in NaCl, and LiCl. Experiments with LiCl were normally conducted last due to occasional closure or instability of PET pores in this electrolyte. However, the order was occasionally changed to confirm the conclusions drawn were not themselves dependent on order. The voltage was scanned between -4 V and +4 V. Current-voltage curves would be recorded at least three times, and average values with standard deviations were calculated.

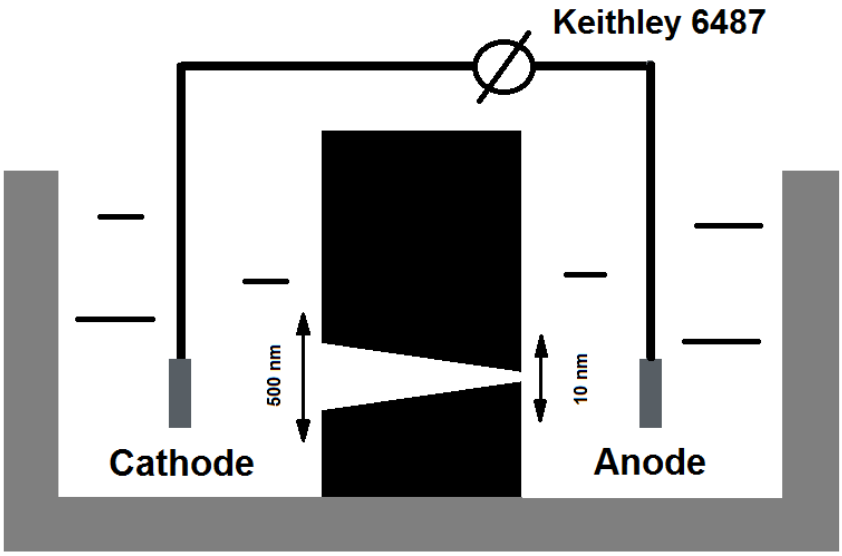

Figure 4.2.1. - Conductivity cell set up for studying electrochemical properties of single conical nanopores. Voltage is applied across the pore and current is recorded using Keithley 6487. Solution resistance is small compared to nanopore resistance thus the voltage drop occurs entirely on the membrane. For ion current measurements, identical Ag/AgCl electrodes are used.

Continuum modeling of ion current through single nanopores was done by Dr. Jan-Frederik Pietschmann from the Technical University in Darmstadt, by numerically solving the Poisson-Nernst-Planck equations with the recently developed software package MsSimPore[47,64]. The package is especially effective in finding convergent solutions in nanopores characterized with high surface densities. Other competing packages (e.g. COMSOL, Inc) show difficulties with convergence when dealing with long, highly charged nanopores. MsSimPore is based on a 1D reduction of the Poisson-Nerst-Planck model and allows for an explicit treatment of the electrolyte reservoirs in contact with the membrane. This package allows high turn around on nanopore computations, which we use to compare to experiment. MsSimPore however does not model atom – atom interactions outside of electrostatics. Every ion is treated

as a point charge. The surface charge density was kept constant in all simulations, and ion diffusion coefficients in the pore were assumed to be equal to their values in a bulk solution found in the literature. We justified the choice by an almost linear dependence of the salts' bulk conductance on concentration up to 2 M. In many regimes this is a powerful tool to use to model our nanopore behavior, and has been done successfully in the past[47]. The modeled conical nanopore had opening diameters of 10 nm and 1000 nm.

Molecular dynamics was used to model a smaller all-atom representation of a conical PET nanopore. This model was adapted from a previous design[63], modified to facilitate comparison with our experiments. The pore had opening diameter of 3 nm and 5nm at the tip and base, respectively. The modeled PET membrane was 10 nm long, 8 nm wide, and 11 nm deep. The boundary conditions were repeated periodically as to produce an extended membrane during the simulation. The size of the pore was reduced compared to the continuum modeling approach and experiment so that the simulation runs were computationally feasible. The surface charge density used was -1 e/nm^2. Simulated pH was 7. The opening angle of the modeled pore was ~15 degrees, which was higher than the 1 to 5 degrees seen in experimentally prepared PET membranes, but allowed to obtain a structure with significantly different opening diameters.

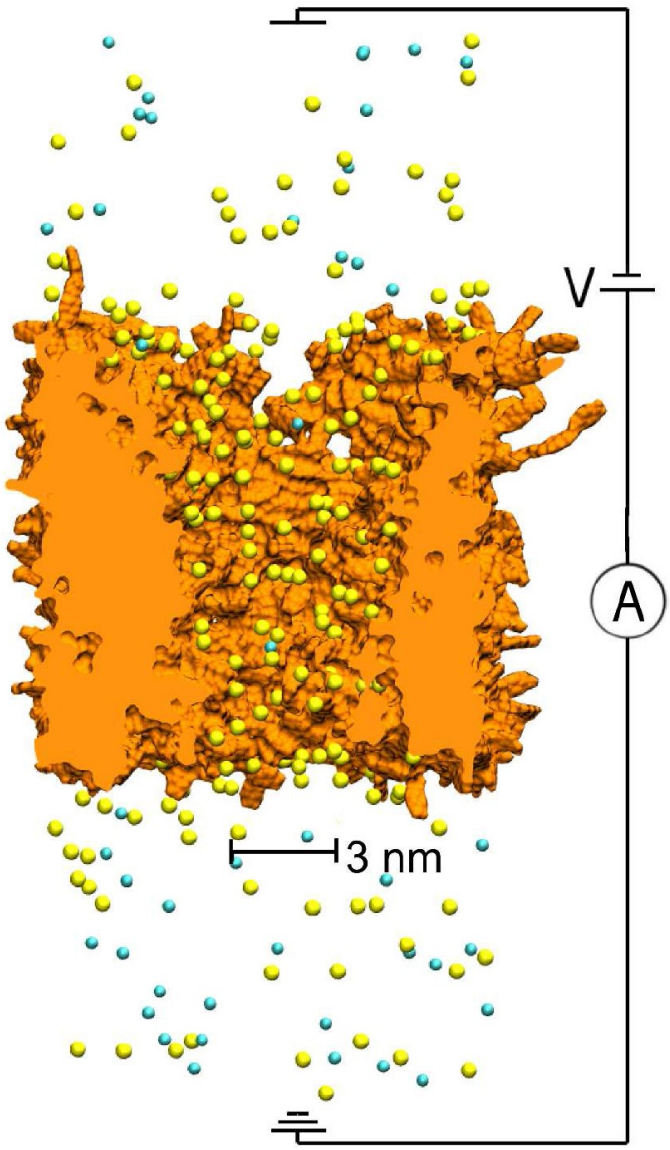

Figure 4.2.2 – All – atom depiction of a conical PET nanopore with electrodes configuration used both in simulations and experiments. Teal spheres represent chloride ions and yellow spheres represent sodium ions, in a concentration of 0.1M. Water molecules are not shown for clarity.

Molecular dynamics is a powerful tool to study atom – atom interactions that occur inside PET nanopores. Each simulation was run for a few tens of ns. The membrane

was solvated by using Visual Molecular Dynamic's (VMD) solvate plugin. 0.1 M bulk concentration was reached by replacing water molecules (randomly selected) by ions. This was done separately for LiCl, NaCl, and KCl solutions. The size of the entire system, solution included, was 26 nm x 8 nm x 11 nm and consisted of 221,778 atoms. An additional three systems consisting solely of 0.1 M bulk solution (KCl, NaCl or LiCl) were prepared, each of dimensions 26 nm x 8 nm x 11 nm with total of 220,542 atoms. These latter systems were used to simulate bulk properties of the salts. Molecular dynamics program NAMD with CHARM36 parameters were used to perform all MD simulations. NBFix corrections were used to accurately describe ion – PET interactions. The timestep used was 2 fs. The cutoff for Van der Walls interactions was 10-12 Å with Ewald full electrostatics computed over a cubic grid with sides of 1 Å length. Rigid hydrogen bonds with periodic boundary conditions were used. The temperature was held at a constant value of 295 Kelvin. A Lowe – Andersen thermostat, 54 rate 50 ps – 1 was used. The PET membrane integrity was restrained (when necessary) by the extrabonds feature of NAMD. The spring constant of each restraint (harmonic and between single carbon atoms and neighboring PET residues) was 0.2 kcal mol 1 A-2. TIP3P water molecule was used in every simulation, and each system was minimized using the conjugate gradient method. Equilibration was achieved within 0.5 ns by using the NPT ensemble. This included constant number of particles, constant pressure, and constant temperature. This was enforced (at 1 atm pressure) by Langevin piston, extendible along the PET pore axis, and with a period of 800 fs. Each system was later simulated in the NVT emsemble (constant particles, volume, and temperature) with a voltage of strength 2 V applied across the pore's main axis. Each salt (KCl, NaCl, and

LiCl) was modeled for both voltage polarities for 20 ns. Symmetric bulk solution systems were also simulated for 20 ns. Furthermore, 20 ns simulations in the absence of any external voltage bias were run, to further characterize the PET nanopore in the presence of the three salts. A steady state was reached in each simulation within 6 ns. Aberrant acceleration of the electro – osmotic flow was prevented by use of the zeromoentum NAMD parameter. System drift was denied by realignment of the PET membrane after simulation. PET has low polarizability, so this effect was not taken into account in simulations. 57 visualization and analysis were performed using VMD 58.

Transport properties of single conically shaped nanopores were first investigated experimentally. Continuum modeling was then completed to shed light on the results expected from an ideal, simplified pore, without complications due to non – electrostatic atom – atom interactions. Molecular dynamics modeling was subsequently performed to elucidate the full ion – surface charge interactions and processes that occur inside PET nanopores.

4.3 Results: Lithium's Unique Behavior Compared to Other Alkali Ions

Current-voltage curves through two conically shaped nanopores at 50 mM of KCl, NaCl and LiCl are shown in Figure 4.3.1. The voltage window was in most cases -4 to 4 V, with 0.1V steps. The recordings in Figure 4.3.1 indicate the pores rectified current with the preferential direction of cation flow from the tip to the wide opening of the pore. Rectification is defined as the ratio of currents recorded in the preferential

direction divided by the current in the opposite voltage polarity. We were surprised to see that rectification degrees of conically shaped nanopores in LiCl were lower compared to the recordings in KCl. This difference is seen in Figure 4.3.2 and is most pronounced in the salt concentrations between 50 mM and 200 mM. Four out of seven examined pores also displayed a difference between rectification in NaCl and KCl; KCl having the higher value. For larger pores (22 and 25 nm) lower rectification degrees in LiCl became pronounced only above 1V. This is explained by voltage – dependent enhancement of ionic concentrations at negative voltages[65,66]. With these pores, the wider opening means larger magnitudes of voltage need to be applied to get a similar cation and anion concentration enhancement compared to the enhancement in smaller pores. The experiments suggest accumulation of lithium ions inside the pore must reach a critical value to lower the magnitude of currents (at negative voltages), which in turn reduces rectification.

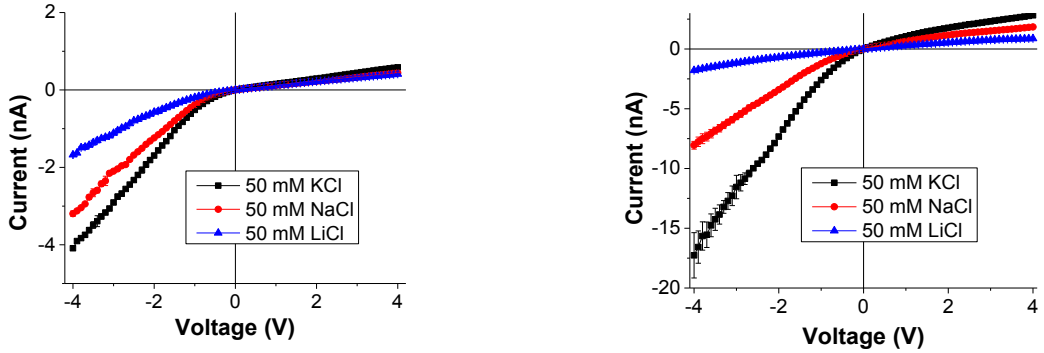

Figure 4.3.1 – Current – voltage curves in 50 mM of KCl (black squares), NaCl (red circles), and LiCl (blue triangles) measured in single conical nanopores with the narrow opening diameter of (a) 9 nm and (b) 14 nm.

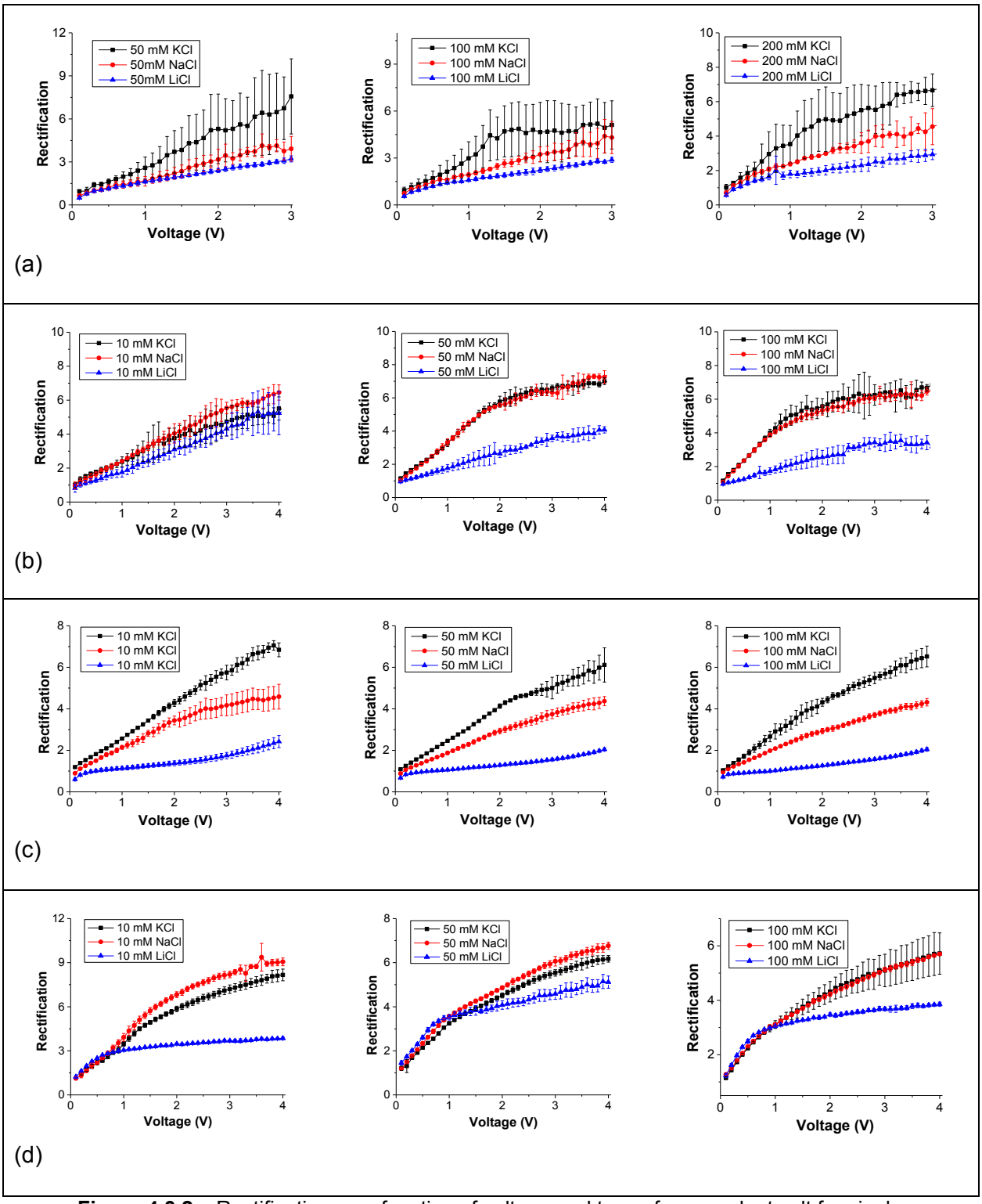

Figure 4.3.2 – Rectification as a function of voltage and type of monovalent salt for single conically shaped nanopores. The tip and wide opening diameters were (a) 4 nm and 350 nm, (b) 9 nm and 300 nm, (c) 14 nm and 520 nm, and (d) 22 nm and 570 nm. A truncated voltage range is displayed for the 4 nm pore due to large fluctuations in currents above 3V; for this pore recordings in 10 mM salt concentration exhibited similar fluctuations, and were therefore omitted.

Relative ion current magnitudes for chloride salts of the three different alkali metals were in order that was expected based on known bulk conductivity and diffusion constants; currents in KCl were the highest, and LiCl currents were the lowest. Ratios of bulk conductivity of the salts and ratios of diffusion coefficients of the cations are shown in Figure 4.3.3, along with the nanopore ion current magnitude ratios. It is clear that the ratios of ion currents in various salts measured in the studied nanopores differed from the values expected based on diffusion coefficient and conductivity ratios.

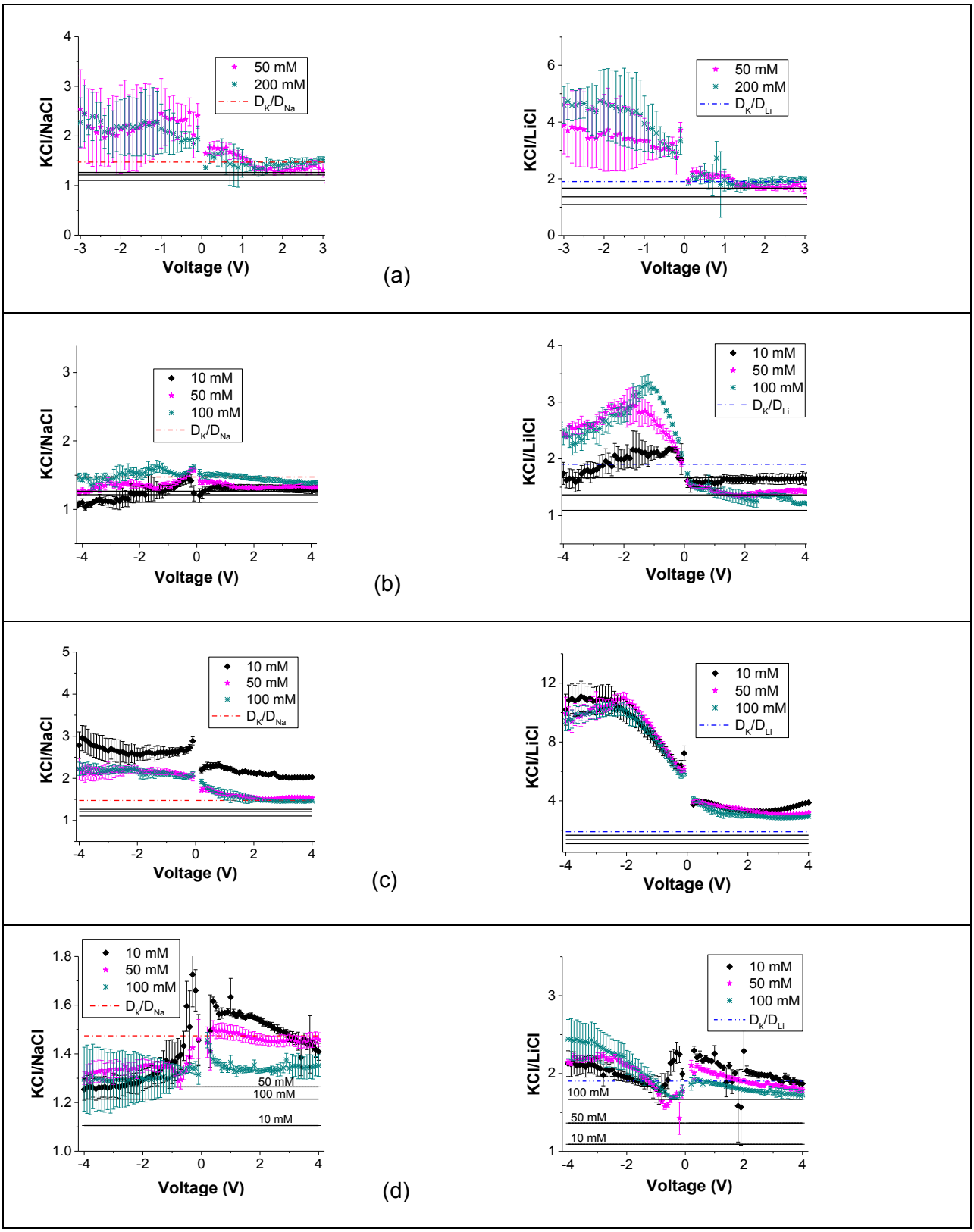
KCl/NaCl
Voltage (V)
50 mM
200 mM
D_K/D_{Na}
KCl/LiCl
D_K/D_{Li}
(a)
10 mM
50 mM
100 mM
(b)
(c)
(d)

Figure 4.3.3 - Ratios of ion current in KCl, NaCl and LiCl recorded in single conically shaped nanopores with an opening diameter of (a) 4 nm, (b) 9 nm, (c) 14nm, and (d) 22nm. Ratios of diffusion coefficients of cations in the bulk as well as ratios of bulk conductivities of salt solutions are shown as well, as dotted and solid lines, respectively.

As shown in Figure 4.3.3 the current ratio KCl / LiCl was always higher than the ratio of currents in KCl and NaCl. This is especially pronounced at negative voltages, where the voltage and surface charge enhance ionic concentrations inside the pore[65,65]. For the 14 nm pore, the KCl / LiCl ratio reached ~11 at 10 mM, while the KCl / NaCl saw a maximum of ~3. Both of these values were well above what bulk properties predicted and suggest currents of these nanopores in LiCl were significantly more reduced compared to the reduction of the current in NaCl. This effect will be further studied with continuum and molecular dynamics modeling.

In order to explain the experimental observations of reduced values of ion current and diminished rectification in LiCl, continuum modeling of ionic transport was performed. As mentioned above, this was done by numerically solving the Poisson-Nernst-Planck equations. The conical pores modeled had a 10 nm tip diameter and 1000 nm opening on the large side, with surface charge set at -1 e/nm^2. Figure 4.3.4 shows current – voltage curves that were returned by the continuum runs, as well as the corresponding rectification versus voltage data. The relative current magnitudes were again in accordance with expectations based on the behavior of bulk salt solutions: currents in KCl were the highest, LiCl currents were the lowest. While the model indeed captured the rectification effect observed with conically shaped nanopores, and the lowest values of currents in LiCl, it could not however reproduce the experimental observation that nanopores in the lithium salt feature the lowest degree of

rectification. In fact, according to the PNP model, LiCl currents are slightly more rectified in comparison to KCl and NaCl currents (Figure 4.3.4).

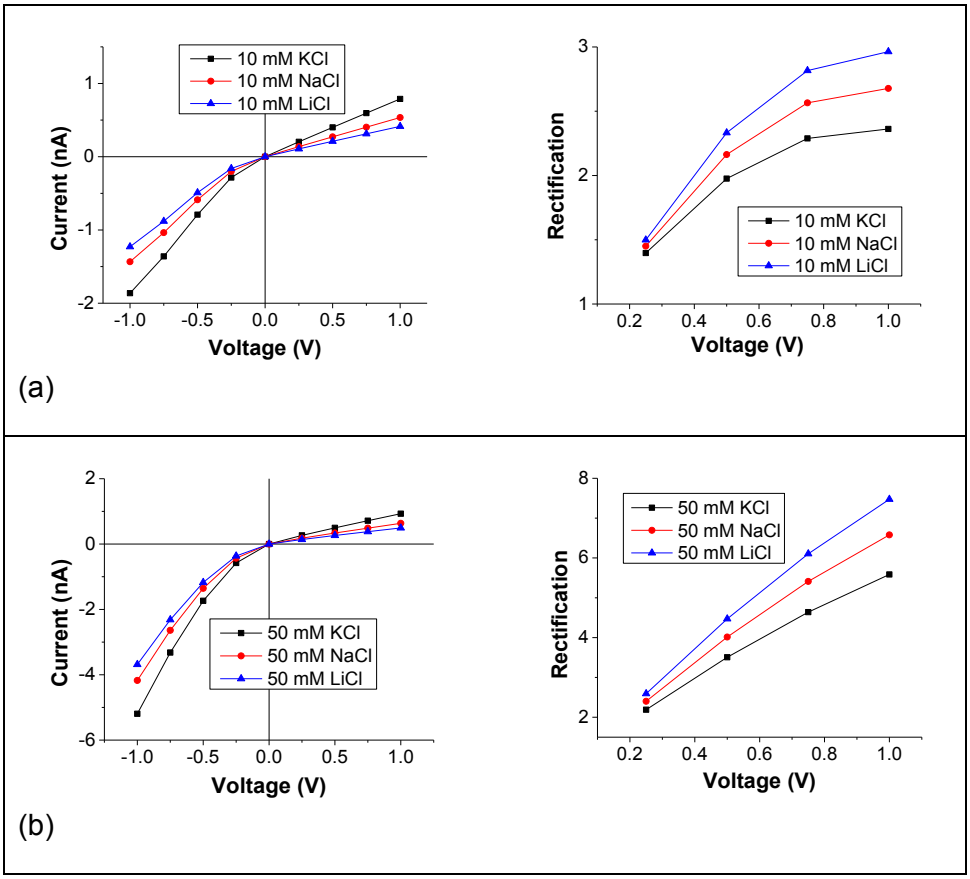

Figure 4.3.4 - Continuum modeling of ion currents through a single nanopore performed by numerically solving the Poisson – Nernst – Planck equations. The modeled pore had dimensions of 1200 nm (length), 10 nm (tip diameter), and 1000 nm (base diameter), with a surface charge density of -1 e/nm^2. Current – voltage curves and rectification versus voltage are shown for (a) 10 mM and (b) 50 mM for KCl, NaCl, and LiCl salts.

The predicted ratios of currents through the modeled pore for selected salts and concentrations are seen in Figure 4.3.5. The current ratios for each molarity and concentration are significantly lower than seen in the experiments (See Figure 4.3.5).

For example in 10 mM salt concentration, the ratio of KCl and LiCl currents observed experimentally in the 14 nm pore was ~5 higher than the ratio of the PNP modeled currents in a 10 nm pore. Moreover, for positive voltages, the modeled ion current ratios approached and eventually matched the ratio of cation diffusion coefficients. For negative voltages on the other hand, the current ratios approached the ratio of the solutions bulk conductivity. The explanation for these observations is based on the voltage-dependence of ionic concentrations in a conical nanopore[65,66]. At negative voltages, concentration of both cations and anions increases so that the pore cation selectivity is lower; as a result, the ratio of currents approaches the ratio of bulk conductivity, determined by both cations and anions. At positive voltages the ionic flow is limited by the formation of a depletion zone whose width increases with an increase in voltage. The depletion zone contains mostly cations, which leads to high cation selectivity of currents measured for positive voltages. As a result, the ratio of positive currents matches the ratio of the cations' diffusion coefficients.

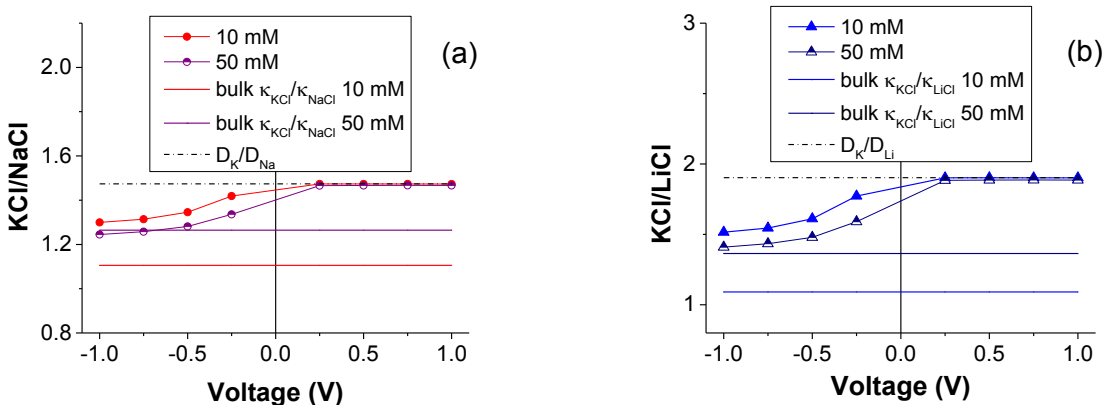

Figure 4.3.5 – Ratios of ion currents in KCl and NaCl (a), and KCl and LiCl (b) as predicted by the continuum modeling based on the Poisson – Nernst – Planck equations. The modeled pore had openings of 10 nm and 1000 nm, respectively. Ratios of bulk conductivities and cation diffusion coefficients are shown as well.

Based on the results shown in Figures 4.3.4 and 4.3.5, we concluded that in order to understand which interactions between ions and the pore walls determine transport properties in various monovalent salts, an atomistic approach needs to be taken. We hypothesized that the experimental results (Figure 4.3.2, 4.3.3) could be explained if lithium ions caused lowering of the effective surface charge of the pores. Modeling these interactions required the specially designed molecular dynamics packages created by Prof. Alexei Askimemtiev at the University of Illinois, Urbana-Champaign. The molecular dynamics approach shows trajectories of each individual ion inside single PET nanopores.

Our first focus was on the on the “dwell time” of each ion next to a charged carboxyl group on the pore walls. Analysis of the trajectories revealed cations would dwell, or bind to the membrane surface, indeed reducing the effective surface charge density on the pore walls. Figure 4.3.6 shows an analysis of this phenomenon. An ion

was considered bound if it remained within 7 Å of the pore wall and failed to move a minimum distance, expected due to diffusion, over a period of time. A frame – by – frame analysis was performed on each cation to determine if it was bound. Its actual displacement was compared to the displacement expected due to diffusion. This minimum displacement, r, was found using $r = \sqrt{6\,D\Delta t}$, where *D* is the diffusion coefficient of an ion, and Δt is the time interval. Results shown in Figure 4.3.6 indicate the number of bound lithium ions is significantly larger than the number of bound sodium and potassium ions. This order matches the order of rectification seen in our nanopores studied in KCl, NaCl and LiCl salts, that is, currents in the lithium salt having the lowest rectification and currents in the potassium salt the highest.

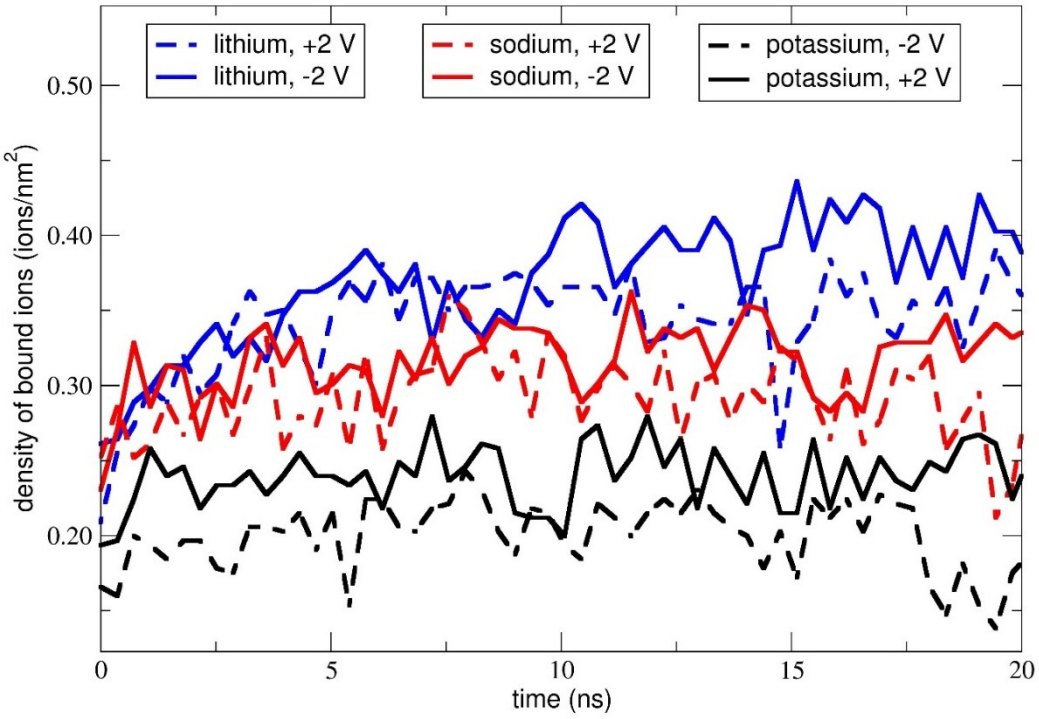

Figure 4.3.6 – Density of bound cations for KCl, NaCl, and LiCl. Simulated results are calculated for -2 and +2 voltages, and displayed versus time. Zero time represents the beginning of the molecular dynamics run.

Another way to analyze the molecular dynamics findings was to map out the effective surface charge inside the nanopore during the molecular dynamics simulations. Seen in Table 4.3.2, lithium is the most effective at lowering the surface charge of the membrane. This corresponds directly with previously stated observation that lithium has the highest density of bound ions out of the three alkali salts tested. It is known from previous studies that surface charge density modulates ion current rectification, and lowering the surface charge can lower rectification of conically shaped nanopores, as discussed in detail in Ref. [47]. All calculations in the previous publication were

performed with the software MsSimpore, and the pores modeled had the same geometry as our experimental pores. Seen in Figure 2.2.4 is the effect of surface charge of a conically shaped nanopore on the pore rectification calculated at 1V. The dependence has a maximum so that lowering of the surface charge initially promotes higher rectification. For surface charge densities lower than the value at which the maximum is reached, lowering of the surface charge densities diminishes the rectification down to a value of 1. The location of the maximum is dependent on the conical pore's dimensions i.e. opening diameters and opening angle. In our experiments, we believe the modulation of surface charge density occurs in the regime at which the rectification increases with the increase of the surface charge density. PET nanopores in contact with LiCl exhibit the lowest experimentally measured rectification degrees, and lithium ions were found to neutralize the surface charge to a larger degree compared to KCl and NaCl.

Salt type	Current-carrying ions	I (nA) at -2 V	I (nA) at 2 V
LiCl	LiCl	-4.49 ± 0.06	6.70 ± 0.05
	Li^+	-4.26 ± 0.06	6.07 ± 0.05
	Cl^-	-0.22 ± 0.04	0.63 ± 0.03
NaCl	NaCl	-4.62 ± 0.06	6.44 ± 0.06
	Na^+	-4.39 ± 0.06	6.21 ± 0.05
	Cl^-	-0.23 ± 0.03	0.23 ± 0.03
KCl	KCl	-6.63 ± 0.07	10.08 ± 0.06
	K^+	-6.57 ± 0.07	10.00 ± 0.07
	Cl^-	-0.06 ± 0.04	0.08 ± 0.04

Table 4.3.1 – – Ion current through a single conical nanopore modeled by MD. Current carried by individual ions was calculated.

Type of electrolyte, 0.1 M	σ (e/nm^2) at -2 V	σ (e/nm^2) at zero bias	σ (e/nm^2) at 2 V
LiCl	-0.64 ± 0.01	-0.61 ± 0.01	-0.66 ± 0.01
NaCl	-0.70 ± 0.01	-0.67 ± 0.01	-0.72 ± 0.01
KCl	-0.78 ± 0.01	-0.77 ± 0.01	-0.82 ± 0.01

Table 4.3.2 – Effective surface charge density of a PET nanopore as modeled by the molecular dynamics approach. With no ion binding the surface charge density is -1 e/nm^2. At each studied external voltage, lithium ions lowered the surface charge density to a greater extent than potassium and sodium ions.

Molecular dynamics allowed us to probe and analyze atomic interactions in a unique way not accessible through any continuum approach. The all-atomistic approach however was not able to predict the direction of rectification correctly, as seen in Table 4.3.3. In contrast to experimental results, currents modeled by molecular dynamics were rectified in the opposite direction so that currents at +2V were higher than currents in -2V. We think it is caused by the low aspect ratio of the modeled pore, since as observed before, rectification is also a function of pore length[47,67,68,69].

Salt type	Current-carrying ions	I_{-2V} / I_{+2V}
LiCl	LiCl	0.670 ± 0.007
NaCl	NaCl	0.719 ± 0.007
KCl	KCl	0.658 ± 0.006

Table 4.3.3 – Rectification degrees of a single conical nanopore as predicted by the molecular dynamics simulations. Rectification degrees smaller than one reveal the opposite direction of rectification compared to that seen with much longer pores used in experiments.

Through combination of experiment, Poisson-Nernst-Planck based continuum modeling, and molecular dynamics, light was shed on lithium's interaction with surface charges in PET nanopores. In comparison to alkali metals potassium and sodium, lithium shows increased binding with negatively charged carboxyl groups in aqueous solution. This

binding lowers the effective surface charge inside the nanopore, observed experimentally as lowering of the ion current magnitude and a decrease in rectification. Our studies have shown that along with multivalent ions, monovalent ions can have a significant effect on ionic current through modulation of the surface charge. Many nanoscale devices such as ionic circuits, artificial ion selective membranes, and nano-transistors depend on homogeneous and sometimes complex surface charge patterns to function. Modulation of these patterns will have large implications on the functionality of these devices. This study elucidates monovalent ions ability to modulate surface charge, so that future researchers can take these effects into account when designing future nanofluidic devices.

Chapter 5

Summary and Conclusions

In this document we described a non-destructive method to probe physical and electrochemical properties of the battery electrode material manganese oxide at the nano and mesoscale. Experiments shown in Chapter 3 were done within the collaborations of the Energy Frontier Research Center (EFRC), to help understand the interactions that cause supercapacitors to underperform. During charge cycling, supercapacitors were achieving only 10 - 25% theoretical capacity[70,71,48]. This observation led our group to design experiments to answer questions about the porosity of the material in aqueous solution. The porosity of the electrode material is important for the process of charging, as it pertains the access of lithium ions to the bulk of the material and might limit the lithium intercalation. In Chapter 4, we shed light on the interactions of three alkali ions with negatively charged carboxyl groups inside PET nanopores, and how those interactions affect rectification. Negatively charged carboxyl groups were known to attract cations, causing the formation of a Debye layer, yet differentiating the level of attraction between the three alkali metals inside PET was a novel experiment. A connection was made between lithium's extended binding time inside PET nanopores and reduction of the pore effective surface charge. It is also possible that the same effect might influence the process of lithium transport in porous manganese oxide and battery charging[42]. These experiments and their resulting

conclusions have spawned ideas for more progressive projects, to further probe properties that become important when reducing the feature size of manganese oxide electrodes to nano-scale dimensions.

When used in nano-architectures, a manganese oxide electrode's behavior differs from what is seen in standard macro-sized electrodes during charge cycling. The increased surface area in nano-architectures allows a higher capacitance per unit gram. Nano-scale features also increase the importance of porosity and selectivity of the electrode material. To help discover the reason manganese oxide under-performs, we embedded a manganese oxide mesorod into cylindrical PET nanopores[42]. We also provided evidence that lithium ions can pass through several thousand nanometers of manganese oxide once a potential is applied across the rod. We have shown that lithium ions can indeed access the interior of an electrode up to ~2500 nm. We also confirmed manganese oxide's surface charge in aqueous solution by recording the electrolyte molarity where current saturation occurred. The current saturation measurement served a dual purpose in that we were able to estimate the diameter of the voids within the manganese oxide matrix to be less than 5 nm. By setting up a concentration gradient, we used the reversal potential measurement to determine that the charge of manganese oxide is negative, adding to knowledge gained from previous zero point charge (ZPC) experiments[54]. Plans are already underway for future use of nanopores to probe structural properties of manganese oxide at various oxidation states. An important future question is therefore how these properties change as the manganese oxide atoms are reduced during charging. Manganese oxide is known to swell as lithium ions intercalate into the material. An increase in void size in our rods is

expected, and will be confirmed in the future studies. It is also unknown how manganese oxide's surface charge is affected by lithium ion intercalation.

Our nanopores were also used to probe the extent and variation in ion-surface charge interactions that occur inside cylindrical and conical PET nanopores. Conical nanopores were used as a test bed to study the effect of lithium, sodium, and potassium's surface charge binding on ion current rectification. Molecular dynamics simulations revealed lithium to have the largest number of ions bound (within 7 Å) to surface charges inside a PET nanopore, in comparison to potassium and sodium[64]. As a result, lithium proved to be most effective at lowering the surface charge density inside the nanopore, and pores in LiCl showed the lowest rectification and currents. The currents in LiCl were also much lower, compared to currents in NaCl and KCl, as well as compared to predictions based on diffusion constants or conductivity values alone. This highlights the importance of understanding interactions between ions passing through the nanopore and the pore walls. As computing power increases, a full length conical PET nanopore should be modeled using molecular dynamics all atom representation. This would allow direct comparison between experiment and modeling, in terms of how rectification properties are affected by lithium's interaction with the surface charge.

Citations

1. Siwy, Z. S. & Davenport, M. Nanopores: Graphene opens up to DNA. *Nat. Nanotechnol.* **5,** 697–8 (2010).

2. Schneider, G. F. *et al.* DNA translocation through graphene nanopores. *Nano Lett.* **10,** 3163–7 (2010).

3. Fischbein, M. D. & Drndić, M. Electron beam nanosculpting of suspended graphene sheets. *Appl. Phys. Lett.* **93,** 113107 (2008).

4. Garaj, S. *et al.* Graphene as a subnanometre trans-electrode membrane. *Nature* **467,** 190–3 (2010).

5. Kalman, E., Healy, K. & Siwy, Z. S. Tuning ion current rectification in asymmetric nanopores by signal mixing. *Europhys. Lett.* **78,** 28002 (2007).

6. Siwy, Z. S., Dobrev, D. D., Neumann, R., Trautmann, C. & Voss, K. Methods of Producing Nanostructures in Membranes and Asymmetrical Membranes. (2005).

7. Dobrev, D., Vetter, J., Neumann, R. & Angert, N. Conical etching and electrochemical metal replication of heavy-ion tracks in polymer foils. *J. Vac. Sci. Technol. B Microelectron. Nanom. Struct.* **19,** 1385 (2001).

8. Apel, P. Y., Korchev, Y. ., Siwy, Z., Spohr, R. & Yoshida, M. Diode-like single-ion track membrane prepared by electro-stopping. *Nucl. Instruments Methods Phys. Res. Sect. B Beam Interact. with Mater. Atoms* **184,** 337–346 (2001).

9. Powell, M. R. *et al.* Nanoprecipitation-assisted ion current oscillations. *Nat. Nanotechnol.* **3,** 51–7 (2008).

10. Bayley, H. Membrane-protein structure: Piercing insights. *Nature* **459,** 651–2 (2009).

11. He, Y. *et al.* Tuning transport properties of nanofluidic devices with local charge inversion. *J. Am. Chem. Soc.* **131,** 5194–202 (2009).

12. Davenport, M., Rodriguez, A., Shea, K. J. & Siwy, Z. S. Squeezing ionic liquids through nanopores. *Nano Lett.* **9,** 2125–8 (2009).

13. Nguyen, G., Vlassiouk, I. & Siwy, Z. S. Comparison of bipolar and unipolar ionic diodes. *Nanotechnology* **21,** 265301 (2010).

14. Li, J. *et al.* Ion-beam sculpting at nanometre length scales. *Nature* **412,** 166–9 (2001).

15. Stein, D., Li, J. & Golovchenko, J. Ion-Beam Sculpting Time Scales. *Phys. Rev. Lett.* **89,** 276106 (2002).

16. Storm, A. J., Chen, J. H., Ling, X. S., Zandbergen, H. W. & Dekker, C. Fabrication of solid-state nanopores with single-nanometre precision. *Nat. Mater.* **2,** 537–40 (2003).

17. Vlassiouk, I., Apel, P. Y., Dmitriev, S. N., Healy, K. & Siwy, Z. S. Versatile ultrathin nanoporous silicon nitride membranes. *Proc. Natl. Acad. Sci. U. S. A.* **106,** 21039–44 (2009).

18. Umehara, S. *et al.* Current rectification with poly-l-lysine-coated quartz nanopipettes. *Nano Lett.* **6,** 2486–92 (2006).

19. Piper, J. D., Clarke, R. W., Korchev, Y. E., Ying, L. & Klenerman, D. A renewable nanosensor based on a glass nanopipette. *J. Am. Chem. Soc.* **128,** 16462–3 (2006).

20. Bruckbauer, A. *et al.* Writing with DNA and Protein Using a Nanopipet for Controlled Delivery. *J. Am. Chem. Soc.* **124,** 8810–8811 (2002).

21. Merchant, C. A. *et al.* DNA translocation through graphene nanopores. *Nano Lett.* **10,** 2915–21 (2010).

22. Howorka, S. & Siwy, Z. S. *Handbook of Single-Molecule Biophysics*. *Handb. Single - Mol. Biophys.* 293 – 339 (Springer US, 2009). doi:10.1007/978-0-387-76497-9

23. Yi, M. & Schnitzer, J. E. Impaired tumor growth, metastasis, angiogenesis and wound healing in annexin A1-null mice. *Proc. Natl. Acad. Sci. U. S. A.* **106,** 17886–91 (2009).

24. Postma, H. W. C. Rapid sequencing of individual DNA molecules in graphene nanogaps. *Nano Lett.* **10,** 420–5 (2010).

25. Kalman, E. B., Vlassiouk, I. & Siwy, Z. S. Nanofluidic Bipolar Transistors. *Adv. Mater.* **20,** 293–297 (2008).

26. Fleischer, R. L., Price, P. B. & Walker, R. M. *Nuclear Tracks in Solids*. (University of California Press, 1975).

27. Silk, E. C. H. & Barnes, R. S. Examination of fission fragment tracks with an electron microscope. *Philos. Mag.* **4,** 970–972 (1959).

28. Eyal, Y. & Gassan, K. Observation of latent heavy-ion tracks in polyimide by means of transmission electron microscopy. *Nucl. Instruments Methods Phys. Res. Sect. B Beam Interact. with Mater. Atoms* **156,** 183–190 (1999).

29. Spohr, R. Method and device to generate a predetermined number of ion tracks. (1983).

30. Fleischer, R. L., Price, P. B. & Walker, R. M. Ion Explosion Spike Mechanism for Formation of Charged-Particle Tracks in Solids. *J. Appl. Phys.* **36,** 3645 (1965).

31. Toulemonde, M., Assmann, W., Dufour, C., Meftah, A. & Trautmann, C. Nanometric transformation of the matter by short and intense electronic excitation: Experimental data versus inelastic thermal spike model. *Nucl. Instruments Methods Phys. Res. Sect. B Beam Interact. with Mater. Atoms* **277,** 28–39 (2012).

32. Vilensky, A. I. *et al.* Thermal regression of latent tracks in the polymer irradiated by high energy heavy ions. *Nucl. Instruments Methods Phys. Res. Sect. B Beam Interact. with Mater. Atoms* **218,** 294–299 (2004).

33. DeSorbo, W. Ultraviolet effects and aging effects on etching characteristics of fission tracks in polycarbonate film. *Nucl. Tracks* **3,** 13–32 (1979).

34. CRAWFORD, W. T., DESORBO, W. & HUMPHREY, J. S. Enhancement of Track Etching Rates in Charged Particle-irradiated Plastics by a Photo-oxidation Effect. *Nature* **220,** 1313–1314 (1968).

35. Romano, J. D. The conical resistor conundrum: A potential solution. *Am. J. Phys.* **64,** 1150 (1996).

36. Zhang, Y., Wang, Y. & Song, Y. Impedance characteristics for solid Ag/AgCl electrode used as recording electric field generated by vessels in seawater. *J. Shanghai Univ. (English Ed.* **13,** 57–62 (2009).

37. Dutta, P. & Beskok, A. Analytical Solution of Combined Electroosmotic/Pressure Driven Flows in Two-Dimensional Straight Channels: Finite Debye Layer Effects. *Anal. Chem.* **73,** 1979–1986 (2001).

38. Kuo, T.-C., Sloan, L. A., Sweedler, J. V. & Bohn, P. W. Manipulating Molecular Transport through Nanoporous Membranes by Control of Electrokinetic Flow: Effect of Surface Charge Density and Debye Length. *Langmuir* **17,** 6298–6303 (2001).

39. Daiguji, H., Oka, Y. & Shirono, K. Nanofluidic diode and bipolar transistor. *Nano Lett.* **5,** 2274–80 (2005).

40. Vlassiouk, I., Smirnov, S. & Siwy, Z. Ionic selectivity of single nanochannels. *Nano Lett.* **8,** 1978–85 (2008).

41. Fick, A. On liquid diffusion. *J. Memb. Sci.* **100,** 33–38 (1995).

42. Gamble, T., Gillette, E., Lee, S. B. & Siwy, Z. S. Probing porous structure of single manganese oxide mesorods with ionic current. *J. Phys. Chem. C* **117,** 24836–24842 (2013).

43. TAKEUCHI, A. & ONODERA, K. Reversal Potentials of the Excitatory Transmitter and L-Glutamate at the Crayfish Neuromuscular Junction. *Nat. New Biol.* **242,** 124–126 (1973).

44. Cervera, J., Alcaraz, A., Schiedt, B., Neumann, R. & Ramirez, P. Asymmetric Selectivity of Synthetic Conical Nanopores Probed by Reversal Potential Measurements. *J. Phys. Chem. C* **111,** 12265–12273 (2007).

45. Goldman, D. E. POTENTIAL, IMPEDANCE, AND RECTIFICATION IN MEMBRANES. *J. Gen. Physiol.* **27,** 37–60 (1943).

46. Hodgkin, A. L. & Katz, B. THE EFFECT OF SODIUM IONS ON THE ELECTRICAL ACTIVITY OF THE GIANT AXON OF THE SQUID. *J. Physiol.* **1,** 37 – 77 (1949).

47. Pietschmann, J.-F. *et al.* Rectification properties of conically shaped nanopores: consequences of miniaturization. (2012). at <http://arxiv.org/abs/1209.4164>

48. Corso, B. L., Perez, I. & Collins, P. G. Electrode Characteristics of Individual, MnO. in 27–33 (2012). doi:10.1149/1.3703510

49. Yan, W. *et al.* Lithographically Patterned Gold/Manganese Dioxide Core/Shell Nanowires for High Capacity, High Rate, and High Cyclability Hybrid Electrical Energy Storage. *Chem. Mater.* **24,** 2382–2390 (2012).

50. Yan, W. *et al.* Mesoporous manganese oxide nanowires for high-capacity, high-rate, hybrid electrical energy storage. *ACS Nano* **5,** 8275–87 (2011).

51. Liu, R., Duay, J. & Lee, S. B. Heterogeneous nanostructured electrode materials for electrochemical energy storage. *Chem. Commun. (Camb).* **47,** 1384–404 (2011).

52. Lou, F. *et al.* Facile synthesis of manganese oxide/aligned carbon nanotubes over aluminium foil as 3D binder free cathodes for lithium ion batteries. *J. Mater. Chem. A* **1,** 3757 (2013).

53. Liu, R., Duay, J. & Lee, S. B. Electrochemical formation mechanism for the controlled synthesis of heterogeneous MnO2/Poly(3,4-ethylenedioxythiophene) nanowires. *ACS Nano* **5,** 5608–19 (2011).

54. Murray, J. W. The surface chemistry of hydrous manganese dioxide. *J. Colloid Interface Sci.* **46,** 357–371 (1974).

55. Ali, M., Ramirez, P., Mafé, S., Neumann, R. & Ensinger, W. A pH-tunable nanofluidic diode with a broad range of rectifying properties. *ACS Nano* **3,** 603–8 (2009).

56. Ali, M. *et al.* Layer-by-layer assembly of polyelectrolytes into ionic current rectifying solid-state nanopores: insights from theory and experiment. *J. Am. Chem. Soc.* **132,** 8338–48 (2010).

57. Apel, P. Y., Blonskaya, I. V, Orelovitch, O. L., Ramirez, P. & Sartowska, B. A. Effect of nanopore geometry on ion current rectification. *Nanotechnology* **22,** 175302 (2011).

58. Kovarik, M. L., Zhou, K. & Jacobson, S. C. Effect of conical nanopore diameter on ion current rectification. *J. Phys. Chem. B* **113,** 15960–6 (2009).

59. Sa, N., Fu, Y. & Baker, L. A. Reversible cobalt ion binding to imidazole-modified nanopipettes. *Anal. Chem.* **82,** 9963–6 (2010).

60. Siwy, Z., Heins, E., Harrell, C. C., Kohli, P. & Martin, C. R. Conical-nanotube ion-current rectifiers: the role of surface charge. *J. Am. Chem. Soc.* **126,** 10850–1 (2004).

61. Hoffmann, J. & Gillespie, D. Ion correlations in nanofluidic channels: effects of ion size, valence, and concentration on voltage- and pressure-driven currents. *Langmuir* **29,** 1303–17 (2013).

62. Kielland, J. Individual Activity Coefficients of Ions in Aqueous Solutions. *J. Am. Chem. Soc.* **59,** 1675–1678 (1937).

63. Bhattacharya, S. *et al.* Rectification of the current in α-hemolysin pore depends on the cation type: The alkali series probed by molecular dynamics simulations and experiments. *J. Phys. Chem. C* **115,** 4255–4264 (2011).

64. Gamble, T. *et al.* Rectification of ion current in nanopores depends on the type of monovalent cations: Experiments and modeling. *J. Phys. Chem. C* **118,** 9809–9819 (2014).

65. Cervera, J., Schiedt, B., Neumann, R., Mafé, S. & Ramírez, P. Ionic conduction, rectification, and selectivity in single conical nanopores. *J. Chem. Phys.* **124,** 104706 (2006).

66. Powell, M. R., Vlassiouk, I., Martens, C. & Siwy, Z. S. Nonequilibrium 1/f Noise in Rectifying Nanopores. *Phys. Rev. Lett.* **103,** 248104 (2009).

67. Cervera, J., Schiedt, B. & Ramírez, P. A Poisson/Nernst-Planck model for ionic transport through synthetic conical nanopores. *Europhys. Lett.* **71,** 35–41 (2005).

68. Wei, C., Bard, A. J. & Feldberg, S. W. Current Rectification at Quartz Nanopipet Electrodes. *Anal. Chem.* **69,** 4627–4633 (1997).

69. White, H. S. & Bund, A. Ion current rectification at nanopores in glass membranes. *Langmuir* **24,** 2212–8 (2008).

70. Hu, L. *et al.* Symmetrical MnO2-carbon nanotube-textile nanostructures for wearable pseudocapacitors with high mass loading. *ACS Nano* **5,** 8904–13 (2011).

71. Fan, Z., Qie, Z., Wei, T., Yan, J. & Wang, S. Preparation and characteristics of nanostructured MnO2/MWCNTs using microwave irradiation method. *Mater. Lett.* **62,** 3345–3348 (2008).